



Empirical prediction of snow and land-fast sea ice temperature from surface meteorology on Pistolet Bay, Northern Newfoundland



Ian D. Turnbull^{a,*}, Reza Zeinali Torbati^b, Rocky S. Taylor^b, Robert S. Pritchett^a

^a C-CORE, Captain Robert A. Bartlett Building, Morrissey Road, St. John's, Newfoundland and Labrador, A1B 3X5, Canada

^b Memorial University of Newfoundland Faculty of Engineering and Applied Science, S.J. Carew Building, 240 Prince Philip Drive, St. John's, Newfoundland and Labrador, A1B 3X5, Canada

ARTICLE INFO

Keywords:

Northern Newfoundland
Land-fast sea ice
Snow on sea ice
Thermodynamic snow/ice modelling

ABSTRACT

The temperature of sea ice and snow cover on the ice surface is a critical component of thermodynamic models of sea ice. Ice temperature is also an important factor in the sea ice strength and therefore in the potential loads the ice can exert on ships, ports, bridges, and offshore structures. The snow layer, while remaining distinct from the sea ice in its physical properties, can become compacted on the ice and contribute to the effective ice thickness and strength. The temperature of sea ice is governed by the atmospheric energy flux balance at the snow surface and the ocean energy flux at the ice base. In addition, snow cover acts as an insulator to sea ice, buffering it against temperature changes due to changes in surface meteorological conditions. The average internal ice temperature and total thickness (through its impact on ice salinity and brine volume) significantly affect ice strength parameters used in the calculation of loads on engineered structures. In February 2017–2019, three field campaigns were carried out on the land-fast ice on Pistolet Bay, north of St. Anthony, Newfoundland in Atlantic Canada. For approximately five days in 2017 and about four days in 2018–2019, surface air temperatures, wind speeds, and snow and ice temperature profiles were continuously measured. Dew point temperatures were obtained from the North American Regional Reanalysis (NARR) dataset. The datasets from the three field campaigns were used to develop empirical linear regression models of snow and ice surface and depth-mean temperatures as a function of the air temperature alone, and of the air and dew point temperatures and wind speed. In this paper, the meteorological data from the three field campaigns are presented, along with the snow and ice thickness and temperature data. The linear models of snow and ice temperature are presented, tested using the observed field data from the Pistolet Bay campaigns, and compared with results obtained from previously published models of snow and sea ice temperature. The results show that the models of snow and ice temperature as a function of the three meteorological variables are modestly more robust than the models as a function of air temperature alone, with R^2 values of up to 0.90. The models presented in this paper have potential usefulness in improved prediction of site-specific snow/ice temperatures and associated temperature-dependent ice properties, such as strength at sites where gridded weather data or in-situ meteorological measurements are available, but in-situ snow/ice temperature measurements are nonexistent.

Introduction

The surface and depth profile temperatures of sea ice and snow cover on the ice are controlled by the energy balances at the surface air-snow and basal water-ice interfaces. While the basal ice temperature is typically about constant around the freezing point of seawater (about -1.8°C), the snow surface temperature can change rapidly in response to surface meteorological variations. Snow cover on the sea ice acts as an insulator and retards temperature changes in the ice. The temperature of

sea ice and snow cover on the ice surface is a critical component of thermodynamic models of sea ice. Ice temperature is also an important factor in the sea ice strength and therefore in the potential loads the ice can exert on offshore structures. The snow layer, while remaining distinct from the sea ice in its physical properties, can become compacted on the ice and contribute to the effective ice thickness and strength.

During February 20–25, 2017 and February 19–23, 2018 and 2019, three field campaigns were carried out on the seasonal land-fast ice which forms each winter over Pistolet Bay, at the northern tip of

* Corresponding author.

E-mail address: ian.turnbull@c-core.ca (I.D. Turnbull).

Newfoundland in Atlantic Canada. The measurement periods covered by the three campaigns totalled 303.7 h or about 12.7 days. While the broader goals of the field campaigns were to characterize the physical ice environment in terms of the snow/ice thermodynamics and ice strength, the results presented in this paper focus on the snow/ice thermodynamics.

In the absence of melting, the temperature of the snow surface is controlled by the energy balance between the downward (incoming) absorbed shortwave and downwelling longwave radiative fluxes, the sensible and latent heat fluxes, and the upward (outgoing) longwave radiative flux from the snow surface (e.g., see [1]; and [2]). In a one-dimensional thermodynamic snow/ice model such as the one presented in Maykut and Untersteiner [1] and Ebert and Curry [2]; the temporal evolution of the vertical temperature profile is therefore mainly governed by the air temperature, humidity, and wind speed at the surface through the impact of these three variables on the aforementioned energy fluxes. Hence, it is possible to predict snow and ice temperatures as a function of solely these three surface meteorological variables.

The field campaigns involved deployment of snow/ice temperature acquisition cables (TACs) which continuously measured vertical temperature profiles, and anemometers which measured surface wind speed throughout the field campaigns. The data loggers for the anemometers and TACs additionally measured the ambient air temperature. After the conclusion of the field campaigns, three-hourly 2 m dew point temperatures were obtained from the North American Regional Reanalysis [3] for the field site location and time periods covering the campaigns. The NARR dataset has approximately a 0.3° (about 33 km) spatial resolution.

The work shown here presents an empirical linear regression model for prediction of snow and ice surface and depth-average temperature as a function of air temperature alone, and as a function of the three measured or reanalysis meteorological variables: the air and dew point temperatures, and the wind speed. The results show that highly robust linear models of snow surface temperature can be obtained for both air temperature and the three weather variables using 5-min averages. The most robust linear models of ice surface and depth-mean snow and ice temperature are obtained using 18-h averages of the three weather variables. The models presented in this paper can be used for prediction of site-specific snow/ice temperatures and the associated ice strength parameters at sites where gridded weather data or in-situ meteorological measurements are available, but in-situ snow/ice temperature measurements are nonexistent.

The shortwave (solar) radiative flux absorbed at the snow surface and the downwelling atmospheric longwave radiative flux also contribute to the energy balance at the snow surface, and therefore to controlling the snow and ice temperature profile. However, the models presented here do not consider these variables explicitly because they could not be measured in the field, and their estimation is highly uncertain. While the time-varying shortwave flux at the top of the atmosphere can be calculated fairly accurately as a function of latitude, season, and time of day, the shortwave radiative flux absorbed by the snow surface is determined partly by the local cloud fractional area and albedo, and the snow surface albedo. Local cloud cover, cloud albedo, and snow albedo could not be measured during the field campaigns, and these variables cannot be estimated with sufficient accuracy for inclusion in the models presented in this paper. While the downwelling longwave radiation was not measured during the field campaigns, the variables which determine this variable are accounted for in the models presented here. Downwelling longwave radiation is a function of the air temperature and the atmospheric humidity through its effect on the atmospheric emissivity (e.g., see [4]).

Bjerkås et al. [5] present results from the STRICE project, in which ice loads on the Lighthouse Norströmsgrund were measured using nine load panels during the winter of 2001. The authors found that 14 global peak loads were correlated with the air temperatures. Timco and Frederking [6] develop a model for predicting the large-scale compressive strength of sea ice sheets, which uses the air temperature, ice thickness, and strain

rate. The authors present an empirical linear model for prediction of the snow-covered ice surface temperature as a function of the air temperature, using two-week average measured air and ice surface temperatures from two locations in the Canadian Arctic spanning one winter season. Their linear model is based on 19 data points, and their depth-mean ice temperature is derived assuming a linear vertical temperature profile in the ice from the surface temperature to the freezing point of seawater (-2°C). Hence, the work presented in this paper is relevant to estimation of ice temperature as a function of air temperature and other meteorological variables. Ice temperature is directly linked to the compressive ice strength (e.g., see [7] and the flexural strength (e.g., see [8] via the ice total porosity and relative brine and air volumes (e.g., see [9], and therefore the loads the ice can exert on structures.

The models presented in this paper could additionally be used to initialize ice-atmosphere boundary layer temperatures in climate modelling, and to validate climate model output. For example, Schenk and Vinuesa [10] used a high-resolution Earth System (climate) Model to explore the large-scale interactions between ice sheets and atmospheric boundary layer flow. The linear models of snow and ice temperature presented in this work could be used to initialize and validate the thermal forcing at specific grid points in such a model's ice sheet at the base of the atmospheric boundary layer.

The paper is organized as follows. Section [Previous studies of snow cover on sea ice, snow/ice temperature, and air temperature-ice strength links](#) presents a review of previously published literature on snow cover on sea ice, snow/ice temperature and thermodynamic analyses and modelling, and studies which explore links between air temperatures and ice strength. Section [Field location, equipment, and methodology](#) describes the location where the 2017–2019 field work was carried out, the equipment used, and how the field measurements were made. Section [Field data sources of uncertainty and measurement error mitigation](#) discusses the possible sources of error in the data recorded in the field due to both natural influences and the instrumentation used, as well as the corrections applied to the data to reduce the effects of sources of error. Section [Meteorological conditions and snow/ice properties](#) summarizes the meteorological conditions and snow/ice temperatures during the 2017–2019 field campaigns. Section [Linear regression models of snow and ice temperature](#) presents some of the key linear regression models for snow and ice surface and depth-mean temperature as a function of air temperature and of the three variables. Section [Model validation and comparisons with other models](#) compares the model predictions for snow and ice temperatures with the 2019 observations, snow and ice temperatures predicted from previously published linear regression models, and with depth-mean snow and ice temperatures predicted from the one-dimensional thermodynamic model. Finally, Section [Conclusions](#) discusses the conclusions of this work, and Appendix A presents additional plots and tables of the meteorological conditions and snow/ice temperatures during the 2017–2019 field campaigns. Appendix A also provides tables of all of the linear regression models for snow and ice surface and depth-mean temperature as a function of air temperature and of the three variables, as well as the comparisons of the model predictions and the observations of snow/ice temperatures from the 2017–2018 seasons.

Previous studies of snow cover on sea ice, snow/ice temperature, and air temperature-ice strength links

Previous studies of snow cover on sea ice have addressed a broad range of topics, from the distribution of snow depths on Arctic sea ice, to time-dependent one-dimensional thermodynamic models of snow and ice temperature, and empirical linear models of snow and ice surface temperature. A number of studies have also linked air temperatures to prediction of ice strength parameters.

Maykut and Untersteiner [1] present the first numerical one-dimensional thermodynamic model of sea ice growth and melt. The authors initialize the model with snow depth, sea ice thickness, and



Fig. 1. The area of Pistolet Bay in which the 2017–2019 field campaigns were carried out is circled in red.

meteorological variables observed in the central Arctic, and run the model for one year. They also test the model sensitivity to snow depth, ice albedo, and ocean heat flux into the base of the ice.

A paper by Ebert and Curry [2] presents a one-dimensional thermodynamic model of sea ice growth and melt that is based on the Maykut and Untersteiner [1] model. The authors add a new parameterization for snow and ice albedo that is dependent upon snow and ice thickness, the solar zenith angle, and whether or not the ice or snow are melting. They also added melt ponds to the model and run the model for one year over the central Arctic.

Li et al. [11] present data collected during two research cruises (one winter and one summer cruise) aboard the RV Nathaniel B. Palmer during 1998–1999 in the Ross Sea, to the northern edge of the Ross Ice Shelf, Antarctica. The authors present empirical linear regression formulas for snow on sea ice surface temperature as a function of air temperature, with R^2 values of around 0.97. They also determine estimates of snow emissivity. A paper by Warren et al. [12] presents long-term measurements of snow depth and density made at Soviet stations drifting on multi-year Arctic sea ice during 1954–1991. The authors tracked the seasonal snow accumulation and melt across the central Arctic basin.

Powell et al. [13] examine the effects of snow and ice properties on the microwave signatures retrieved from airborne observations of snow depth on sea ice in the Beaufort and Chukchi Seas near Barrow, Alaska during March 2003. The snow depths are validated with ground-based measurements. A companion paper by Sturm et al. [14] presents snow depth and ice thickness measurements from the same field sites as those in Powell et al. [13].

Haas et al. [15] present data collected on an ice floe in the Weddell Sea over five weeks during November–January 2004–2005 during the spring seasonal warming. Through the use of helicopter and ground-based electromagnetic (EM) induction ice thickness and ruler-stick snow thickness measurements, changes in the floe thickness, snow temperature, and ice temperature, salinity, and brine volume were monitored.

Lecomte et al. [16] present a new and improved one-dimensional thermodynamic scheme for the snow layer in the Louvain-la-Neuve sea-Ice Model (LIM). They validate the model with data from Point Barrow, Alaska and a location in the western Weddell Sea, offshore Antarctica. Prinsenberg et al. [17] present snow and ice thickness data from a survey of Lake Melville in Labrador in March 2009. Ice thickness data were collected via a helicopter-borne EM induction sensor, and snow thickness was collected via ground-penetrating radar (GPR). A paper by Tonboe et al. [18] presents results of model simulations of snow surface temperature on sea ice and the microwave effective temperature. The authors present a linear regression model for snow surface temperature on sea ice as a function of the 2 m air temperature.

Haapala et al. [19] present data on the small-scale (*e.g.*, hundreds of meters) variability of snow and sea ice thickness on first-year ice north of Svalbard in the Norwegian High Arctic. The authors show that this small-scale variability in snow depth is sufficient to affect freeboard calculations as a function of ice thickness. Raleigh et al. [20] present data on land-based snow surface temperature as a function of air temperature and humidity (*e.g.*, dew point temperature), and emphasize the importance of atmospheric humidity in the snow surface energy balance. The authors suggest that these atmospheric datasets could be used to predict snow surface temperatures in remote regions such as on sea ice.

A paper by Castro-Morales et al. [21] presents a model to simulate snow depth on Arctic sea ice and its spatial distribution and variability. The model accumulates snow on sea ice in proportion to the ice thickness. The model overestimates snow depth compared to measurements, on the order of a few cm. Kwok et al. [22] present comparisons of several datasets of springtime snow depth measurements on Arctic Sea ice as obtained by radar from the Operation IceBridge campaign flights. Lu et al. [23] present 10 years of data from lidar measurements of snow and sea ice aerial coverage over the Arctic to study both the seasonal and inter-annual variabilities in these parameters.

Finally, Merkouriadi et al. [24] discuss the role of snow cover on the growth of sea ice using data collected on a research cruise in 2015 north



Fig. 2. A D405 data logger connected to three TACs deployed through the snow and land-fast sea ice.

of Svalbard. The authors use a one-dimensional snow and ice thermodynamics model forced with reanalysis data to show that snow accumulation on second-year ice contributes to its thickening through the formation of snow-ice, even in the absence of any basal ice growth.



Fig. 3. Example of a snow pit dug adjacent to a TAC for measurement of snow thickness on the ice.

Field location, equipment, and methodology

The field work in all three years was carried out on Pistolet Bay at the northern end of the eastern Canadian island of Newfoundland which opens to the north into the Strait of Belle Isle (see Fig. 1). This site was chosen due to its relative ease of access and the reliably annual formation of land-fast sea ice which freezes across the entire bay each winter. The field work site was at a location in the northeastern corner of the bay, approximately 500 m offshore at around 51.55°N, 55.75°W.

Two BeadedStream D405 data loggers were deployed at the field site, each connected to three 1-m long Temperature Acquisition Cables (TACs) (see Fig. 2). The cables connecting the TACs to the data loggers were protected by a polyurethane jacket. The six TACs each contained 41 temperature sensors housed in a fiberglass jacket, with 2.5 cm spacing between each sensor, and each TAC was placed in a hole drilled through the snow and ice to the water below. The D405 data loggers were mounted approximately 1 m above the snow surface. The data loggers were housed in PVC plastic and sealed to an IP67 watertight rating.

The temperature sensors on the TACs have a 0.1 °C accuracy and 0.01 °C precision. The D405 data loggers were programmed to record the vertical temperature profile from each TAC every 5 min throughout each of the two field programs, as well as the internal temperature of the logger (also at 0.1 °C accuracy). Once per day, the following measurements and time of measurement were taken manually for each TAC: the distance from the top temperature sensor to the snow surface, and the snow depth adjacent to the TAC, using a meter stick (see Fig. 3).

Adjacent to each of the two D405 data loggers, an ice thickness measurement was made once daily with a Kovacs T-bar ice thickness measuring tape. In order to ensure that only the ice thickness was measured, the surface surrounding the thickness hole was first cleared of snow. These measurements allowed for determination of TAC location in the depth profile (e.g., the snow-air, snow-ice, and ice-water interfaces).

Wind speed was measured at a height of approximately 1.4 m above the snow surface using two Davis Pro anemometers mounted on tripods (see Fig. 4). The anemometers were each connected to a Logic Energy data logger which recorded 1-min average wind speeds (1 ms^{-1} accuracy and 0.01 ms^{-1} precision) and internal temperatures (0.1 °C accuracy and 0.01 °C precision). The wind data loggers were housed in a sealed (IP65



Fig. 4. A Davis Pro anemometer connected to a data logger.

watertight rating) plastic case.

The TACs and anemometers were deployed in a line across the ice, with each instrument approximately 15 m apart from the next (see Fig. 2). The reasons for deploying multiple instruments of each type were to achieve data redundancy in case of instrument malfunction, and to obtain average temperature and wind speed readings for the field site. After each field campaign, the data were linearly interpolated to a common time-series with 1-min time-steps. For each time-step, the wind speeds were averaged between the two anemometers, the internal logger temperatures were averaged between the two TAC D405 and anemometer data loggers (this was assumed to represent ambient air temperature at the field site), and the snow surface temperatures and ice surface temperatures were averaged between the six TACs. In addition, for each TAC and each time-step, the average snow temperature with depth was calculated, as well as the average ice temperature with depth. The average snow and ice temperatures were subsequently averaged between the six TACs at each time-step. In this way, spatially averaged wind speeds, air temperatures, snow and ice surface temperatures, and snow and ice depth-mean temperatures could be estimated for the field site. Averaging data between instruments and their exact locations also helps to mitigate the effects of possible measurement biases introduced by individual instruments and their point-specific deployment locations.

Field data sources of uncertainty and measurement error mitigation

This section discusses possible sources of error in the data recorded in the field due to both natural influences and the sensors themselves, as well as the corrections applied to the data to mitigate the potential effects of sources of error. First, the manner in which ice thickness was measured with a T-bar thickness gage and drilling a hole on top of which some slush would immediately freeze, meant that ice thickness is considered to be within possible error bars of ± 1 cm. Efforts were made to mitigate the potential impact of this source of error by brushing away as much slush as possible from the point on the ice surface where the T-bar ice thickness gage would make contact.

Second, the manner in which ambient air temperature was measured could have introduced a transient positive bias in the measurements for short periods (e.g., on the order of a couple of hours per day), as well as a potential time-lag in the measurements compared to the actual air

temperature. Both the temperature and wind data loggers measured internal temperature, which means the temperature sensors were not directly exposed to the air. This may have led to a small time-lag between changes in actual air temperatures at the field site and the instrument internal temperatures being measured due to possible insulating effects of the instrument housing. The instrumentation housing materials for the wind versus the temperature data loggers would also most likely have different thermal conductivities, leading to different time lags between the outside ambient air temperature and internal logger temperature.

In addition, direct sunlight on the instrument housing during the early afternoon hours on days with minimal cloud cover had the potential to bias ambient air temperature measurements to be somewhat higher due to potential heating of the instrument housing. However, the longer periods of time-averaging applied to the data and discussed in Section [Linear regression models of snow and ice temperature](#) most likely helped to mitigate the effects of the instrument housing on potential time-lag in the recorded ambient air temperatures. The averaging of data between multiple sensors would additionally serve to mitigate the potential positive temperature bias effects of the instrument housing due to the different intensities of direct sunlight each of the data loggers would receive at any one time (e.g., the exact angle at which sunlight would contact each instrument would necessarily be different due to the placements of the instruments relative to one another).

Third, there exists a likely source of uncertainty in the measurements of snow depth. While snow depth was measured within several cm of each TAC (e.g., see Fig. 3), the precise snow depth at each TAC could have been different from the measurements by ± 1 cm. Snow depth on sea ice varies both spatially and temporally due to continual blowing and drifting across the ice pack. The TACs form a natural barrier to snow blowing across the ice, leading to small drifts piling up against the TACs on the windward side. While snow depth was only measured once per day, the actual snow depth at each TAC could have varied on the order of ± 1 cm between measurements due to the near-constant transport of snow across the ice pack. Since the spacing of the temperature sensors on the TACs is only 2.5 cm, determination of the exact location of the snow surface on the TAC is important for proper measurement of the snow surface temperature at the correct sensor. While blowing and drifting snow can lead to excess snow piling temporarily up against a TAC

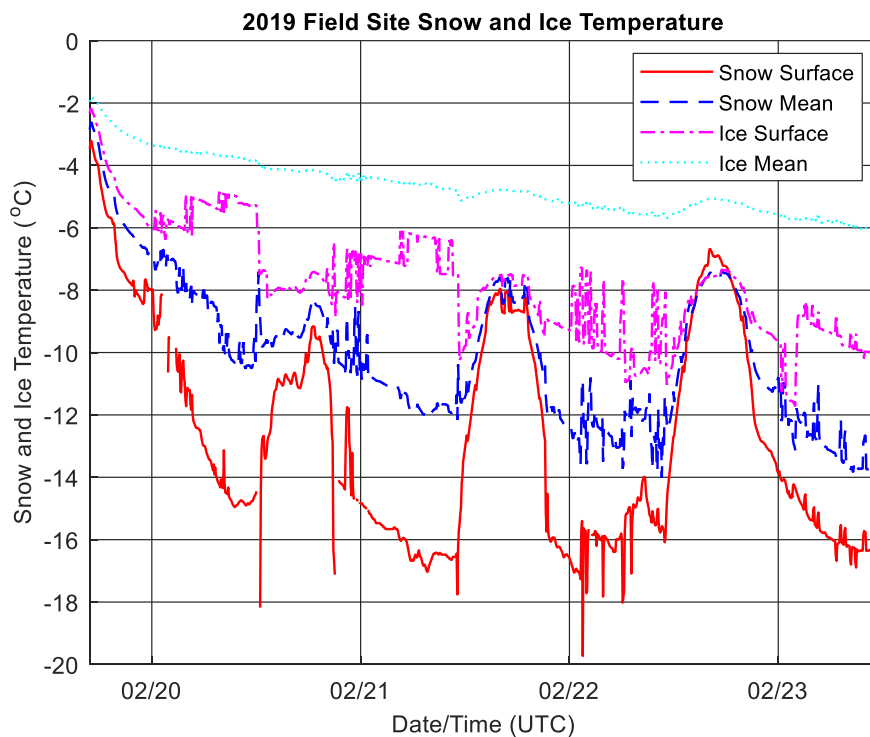


Fig. 5. Snow surface, depth-mean snow, ice surface, and depth-mean ice temperatures at the field site during the 2019 campaign.

between snow depth measurements, this phenomenon can also reduce snow depth at a TAC site and leave TACs exposed to air that are assumed to be buried in snow. TACs exposed to air are also subject to the potential positive bias in temperature readings when exposed to direct sunlight. However, as was done with the air temperature measurements, the averaging of snow surface temperatures between TACs would have most likely mitigated the errors introduced by the changing snow depths

across the field site. The data time averaging (e.g., see Section [Linear regression models of snow and ice temperature](#)) would additionally mitigate the potential effects of rapid changes in snow depth due to blowing and drifting. Moreover, visual observations of snow around the instrumentation deployment sites indicated that the instruments did not appreciably affect the local distribution of snow around the TAC and this factor is therefore not believed to have a significant influence on results.

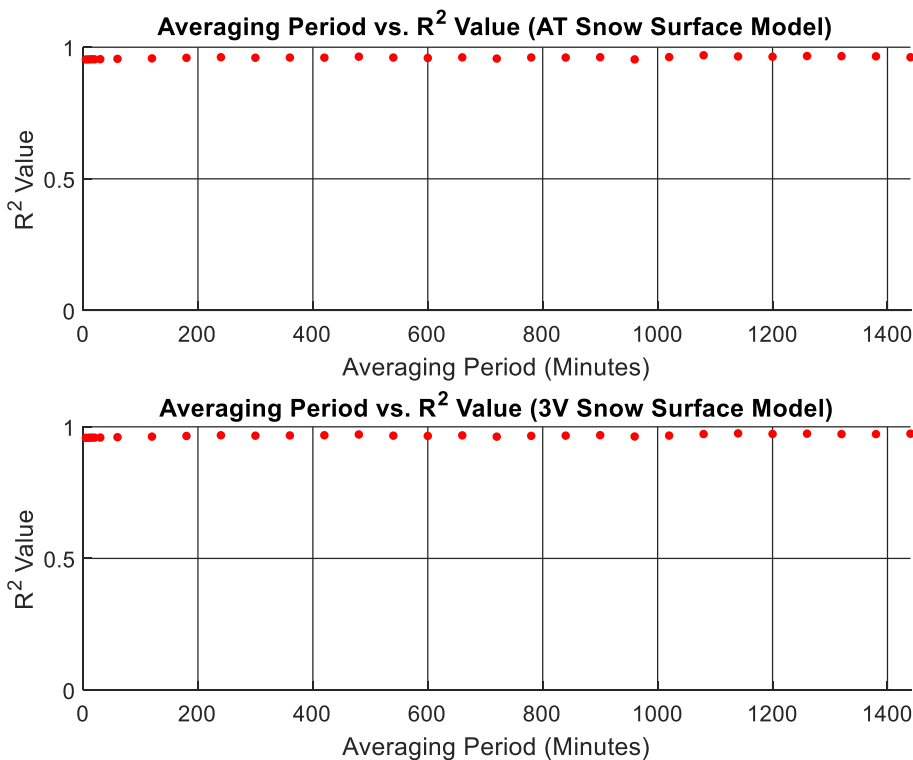


Fig. 6. Variable averaging period vs. R^2 value for AT and 3 V snow surface temperature linear regression models.

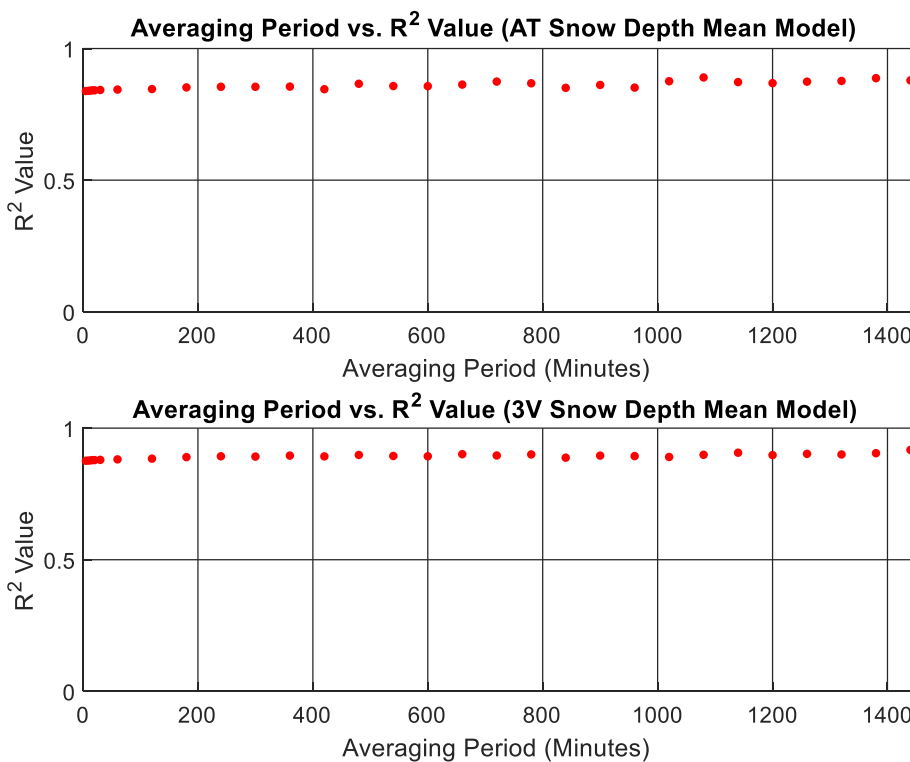


Fig. 7. Variable averaging period vs. R^2 value for AT and 3 V snow depth-mean temperature linear regression models.

Meteorological conditions and snow/ice properties

Average snow depth at the TAC locations varied significantly between the three field campaigns (see Figure 22 in [Appendix A](#)). Snow depth was linearly interpolated between daily measurements. During the 2017 campaign, very little new snow fell, but blowing and drifting caused the

increase in the mean snow depth at the TACs. About 1 cm of new snow fell during the 2018 campaign, and blowing and drifting caused a decrease in snow depth during the 2019 campaign.

Surface air temperatures during the 2017 field campaign were relatively mild with three periods in which the temperature rose above 0 °C (see Figure 23 in [Appendix A](#)). Temperatures during the 2018 and 2019

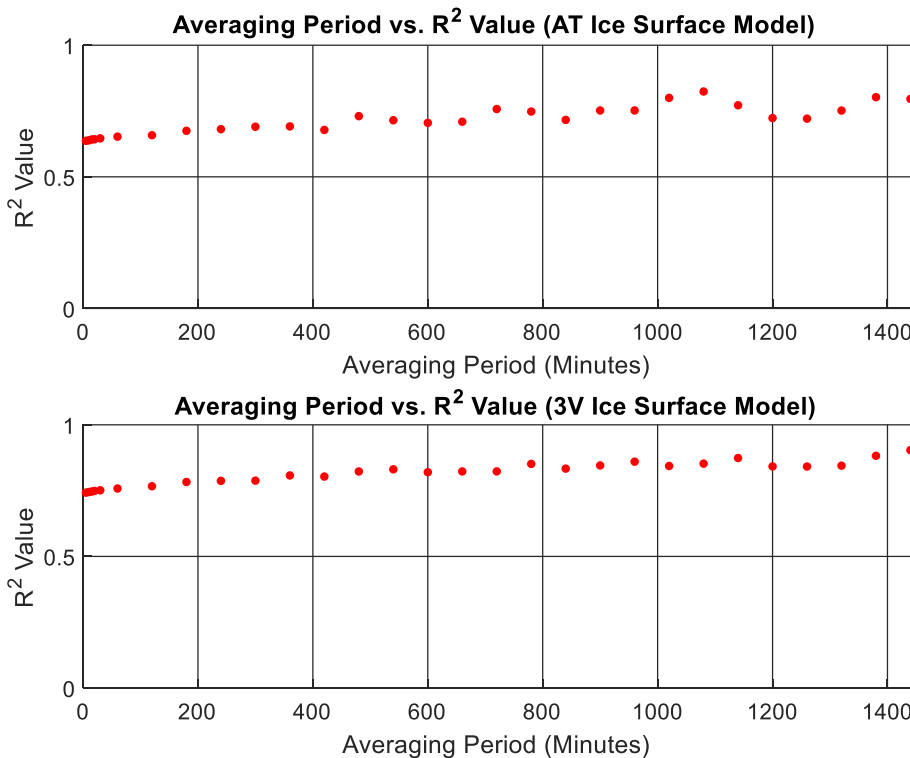


Fig. 8. Variable averaging period vs. R^2 value for AT and 3 V ice surface temperature linear regression models.

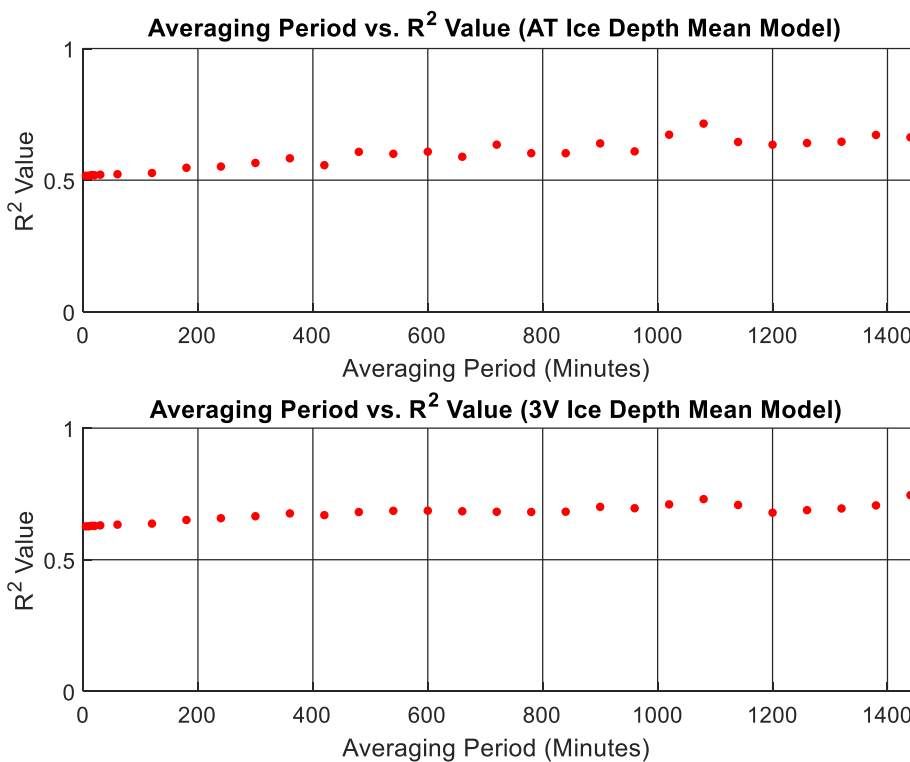


Fig. 9. Variable averaging period vs. R^2 value for AT and 3 V ice depth-mean temperature linear regression models.

campaigns were much colder with only one brief period above 0 °C observed at the beginning of the 2018 campaign. Similarly, dew point temperatures during the 2018 and 2019 campaigns were significantly colder than during the 2017 campaign (see Figure 24 in [Appendix A](#)). The periods with above-freezing air temperatures are not considered in the development of the models for snow and ice temperatures presented in this paper. Wind speeds during the three field campaigns were highly variable, and were strongest during the 2018 campaign, followed by 2019 (see Figure 25 in [Appendix A](#)).

[Fig. 5](#) shows the snow and ice surface and depth-mean temperatures measured during the 2019 campaign (see Figure 26 and Figure 27 in [Appendix A](#) for similar time-series plots from the 2017–2018 campaigns). As expected, the snow surface temperatures show the greatest variability as they responded most sensitively to the surface meteorology. The ice depth-mean temperatures show the least variability as they are the most insulated from the variable weather conditions at the snow-air interface. Table 2 in [Appendix A](#) summarizes the statistics for all the meteorological variables and snow and ice properties discussed in Section [Meteorological conditions and snow/ice properties](#) for the three field campaigns.

Linear regression models of snow and ice temperature

In this section, linear least-squares regression models are presented for snow and ice surface and depth-mean temperatures. For each predictand (e.g., snow surface temperature, depth-mean snow temperature, ice surface temperature, and depth-mean ice temperature), a model as a function of only air temperature is presented (hereafter referred to as the air temperature or AT models), along with a companion model as a function of three meteorological variables (e.g., the air and dew point temperatures and the wind speed; hereafter referred to as the three-variable or 3 V models). This allows for prediction of snow and ice temperatures under circumstances of variable availability of meteorological data, as well as showing the improvement in model predictions when the three meteorological variables are used as opposed to only using the air temperature.

[Fig. 6](#) through [Fig. 9](#) show the averaging periods versus the resulting linear model R^2 values, and Table 3 through Table 6 in [Appendix A](#) present the model R^2 values, slopes, and intercepts for the AT and 3 V snow surface, snow depth-mean, ice surface, and ice depth-mean temperatures, respectively. The averaging periods start at 5 min, the resolution of all temperature measurements, then increase to 10, 15, 20, 30, and 60 min, followed by hourly increments to 24 h. Note that since the temperatures were recorded at 5-min intervals, 5-min average temperatures essentially represent the linearly interpolated midpoints between measurements.

The R^2 values in [Fig. 6](#) show that the statistical robustness of the snow surface temperature models does not change significantly for large versus small averaging periods, which indicates that a 5-min averaging period is sufficient for prediction of snow surface temperature. This result is unsurprising given the fact that the snow surface is in direct contact with the atmospheric boundary layer, and therefore responds rapidly to changes in it. In addition, the fact that the R^2 values do not vary significantly between the AT and 3 V models indicates that air temperature alone is a robust predictor of snow surface temperature.

However, the models for temperatures in the layers which are more insulated from the overlying atmosphere and therefore respond more slowly to changes in the atmospheric boundary layer all show a small positive correlation between R^2 value and averaging period ([Fig. 7–9](#)). The correlation is particularly pronounced for the ice surface and depth-mean temperature models. The models for these layers additionally show a larger discrepancy between R^2 values for the AT and 3 V models for a given averaging period, with R^2 values consistently higher for the 3 V models. The positive trend in R^2 value versus averaging period and the difference in R^2 values between the AT and 3 V models is most pronounced for the ice depth-mean temperature ([Fig. 9](#)).

Although readers may choose to further test any of the models presented in Table 3 through Table 6 in [Appendix A](#), this paper further evaluates only selected models from these tables. For the snow surface temperature, the 5-min average models are selected. The models for the layers below the snow surface were selected according to the following three criteria: first, the R^2 value for the 3 V model must be maximized,

Table 1

Selected AT and 3 V models for snow and ice surface temperatures and depth-mean snow and ice temperatures, and T11 snow surface temperature and TF90 ice surface temperature models.

Model	Averaging Time	Formula	R ² Value	Modelled vs. Observed RMSE (°C)
Snow Surface Temperature (°C)	5 Minutes	T _{ss} = 0.7017T _a - 1.6429	0.95	0.98
		T _{ss} = 0.6082T _a + 0.1075T _d - 0.024W _s - 0.746	0.96	0.93
		(T11) T _{ss} = 1.14(T _a + 273.15) - 311.09	0.29	3.83
Snow Mean Temperature (°C)	18 Hours	T _{sm} = 0.5998T _a - 0.5899	0.89	1.10
		T _{sm} = 0.3672T _a + 0.1803T _d - 0.1995W _s + 0.8934	0.90	1.05
Ice Surface Temperature (°C)	18 Hours	T _{is} = 0.3607T _a - 2.1652	0.82	0.87
		T _{is} = 0.0272T _a + 0.2902T _d - 0.0544W _s - 0.7346	0.85	0.79
		(TF90) T _{is} = T _a , -2 ≥ T _a ≥ -10; T _{is} = 0.6T _a - 4, T _a < -10	0.00	4.10
Ice Mean Temperature (°C)	18 Hours	T _{im} = 0.1957T _a - 1.56	0.71	0.64
		T _{im} = 0.1194T _a + 0.0531T _d - 0.1098W _s - 0.8961	0.73	0.63

second, in the event a maximum R² value occurs more than once, the model with the smallest averaging period with the maximum R² value must be selected, and third, the coefficients for the air and dew point temperatures must be positive while the wind speed coefficient must be negative. The third criterion ensures the models are physically sound. Logically, there should be a positive correlation between air or dew point temperature and the temperature of the snow or ice. Higher dew point temperatures correspond to high atmospheric humidity, which slows the rate of heat loss from the snow and ice through its effects on the latent heat and downwelling longwave radiative fluxes. In sub-freezing air temperatures, there should be a negative correlation between wind speed and snow or ice temperature due to the effect of wind speed on sensible heat loss from the snow surface.

Using these criteria, the R² values for the 3 V models all peak at a minimum averaging period of 1080 min or 18 h. These criteria were used in order to select models which are as statistically robust as possible and physically sound, while maximizing their temporal resolution and therefore their utility in predicting changes in snow and ice temperatures and associated strength parameters with time. In addition, this rather significant length of time averaging allows for the depth-mean snow temperature to be robustly predicted independent of variations in snow depth of several cm which were observed at the field site in all three campaigns and between the campaigns (e.g., see Figure 22 in Appendix A). This averaging period also allows adequate time for the full snow and ice temperature profiles to respond to changes in surface meteorological conditions.

Table 1 presents the selected models for snow and ice surface and depth-mean temperature as a function of the surface meteorology. In addition, the AT models presented here for snow and ice surface temperature are compared with the AT model for snow surface temperature presented in Tonboe et al. [18] (hereafter referred to as T11) and the model for snow-covered ice surface temperature presented in Timco and Frederking [6] (hereafter referred to as TF90). Also shown are the modelled versus observed predictand root-mean-square-error (RMSE). In Table 1, all temperatures are in °C, wind speed is in ms⁻¹, and radiative fluxes are in Wm⁻².

The results in Table 1 show that application of the T11 model to the 2017–2019 datasets for air and snow surface temperatures produces a

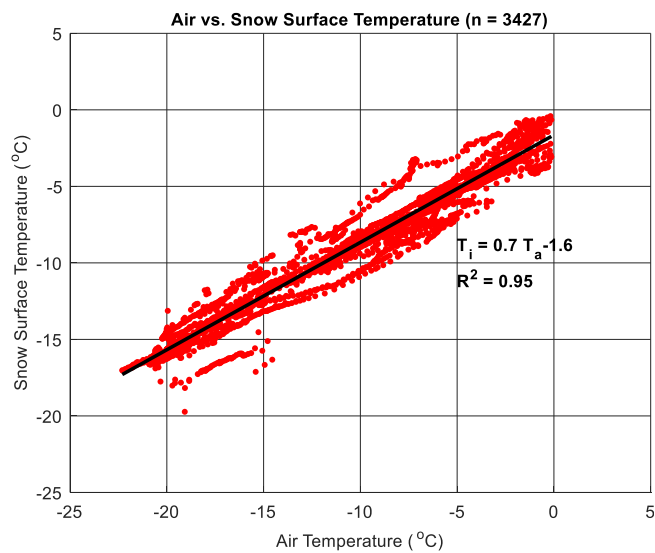


Fig. 10. Five-minute average air vs. snow surface temperature from the 2017–2019 campaigns.

significantly lower R² value and higher RMSE compared to the AT and 3 V snow surface temperature models developed in this paper. The AT and 3 V models for depth-mean snow temperature produce similar R² values and RMSE values. The air temperature coefficients in both models for depth-mean snow temperature suggest that the air temperature is the dominant control on this variable at 18-h averages. The dew point temperature and wind speed each have coefficients of similar magnitude, which suggests that neither of these variables dominates over the other's effect on the depth-mean snow temperature.

Application of the AT and 3 V ice surface temperature models to the 2017–2019 datasets produces a significantly smaller RMSE compared to the TF90 air temperature model. This result shows that while the TF90 model was generated using two-week averaging, the new AT and 3 V models presented here are more reliable for prediction of ice surface temperature at a much higher temporal resolution. The 3 V model for ice surface temperature suggests that the dew point temperature is the dominant control on this variable at 18-h averages, with the air temperature and wind speed exerting control at similar magnitudes but an order smaller than the dew point temperature.

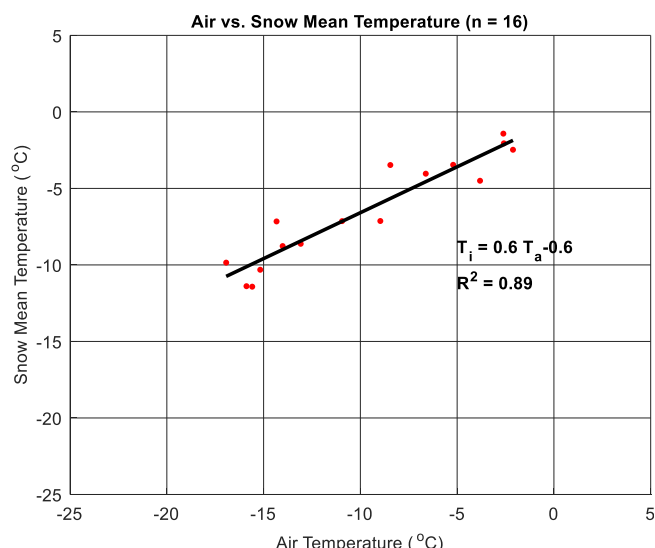


Fig. 11. Eighteen-hour average air vs. depth-mean snow temperature from the 2017–2019 campaigns.

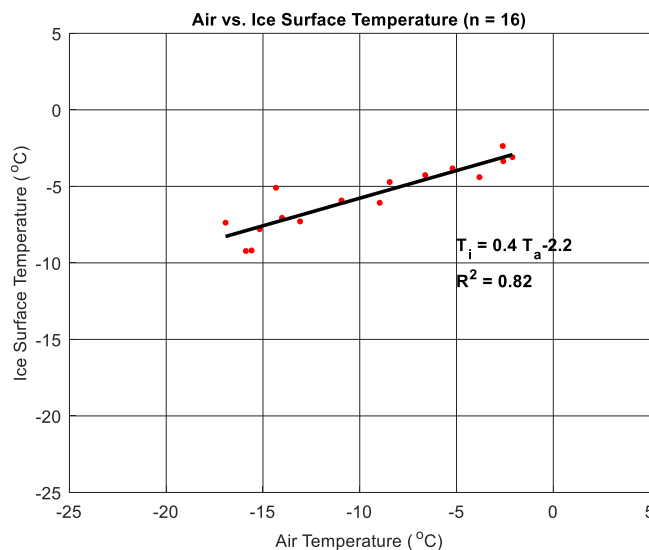


Fig. 12. Eighteen-hour average air vs. ice surface temperature from the 2017–2019 campaigns.

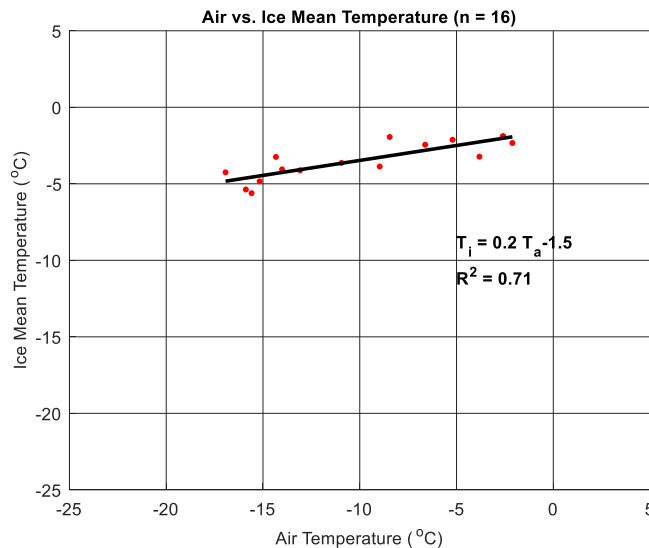


Fig. 13. Eighteen-hour average air vs. depth-mean ice temperature from the 2017–2019 campaigns.

Of the four predictands presented in Table 1, the depth-mean ice temperature responds the slowest to changes in the surface meteorological conditions. This is due to the fact that the ice profile is buffered against the surface atmospheric conditions by the snow layer, and the fact that it takes more time to transmit energy through the full ice thickness profile compared to the response time of the energy balance at the ice surface. Using an 18-h averaging time, the AT and 3 V models produce similar R^2 values and RMSE values. Given the fact these models were generated using two datasets with average ice thicknesses which differed by up to 17 cm (e.g., see Table 2 in Appendix A), the linear regression models for depth-mean ice temperature given in Table 1 can be used independent of ice thickness for thicknesses up to 65 cm (e.g., the maximum ice thickness measured in the three campaigns). The 3 V model for depth-mean ice temperature suggests that the air temperature and wind speed are the dominant controls on this variable at 18-h averages, with the dew point temperature coefficient approximately equivalent to half of the air temperature and wind speed coefficients.

Fig. 10 through Fig. 13 show the time-averaged (as per Table 1) air versus snow surface, depth-mean snow, ice surface, and depth-mean ice

temperatures from the 2017–2019 field campaigns, respectively, as well as the associated air temperature linear regression models and associated R^2 values (see Fig. 12) (see Fig. 11).

Model validation and comparisons with other models

In this section, the models presented in Table 1 are validated for the time-series of snow and ice surface and depth-mean temperatures from the 2017–2019 field campaigns. The results of the AT and 3 V snow and ice depth-mean temperature models are compared with depth-mean snow and ice temperatures calculated from numerical integration of the one-dimensional heat flux equation in the temporal evolution of a snow and ice depth-temperature profile (hereafter referred to as the thermodynamic model). The one-dimensional heat flux equation for snow and ice is given as (e.g., [2]; and [1]),

$$(\rho c)_{i,s} \left(\frac{\partial T_{i,s}}{\partial t} \right) = k_{i,s} \left(\frac{\partial^2 T_{i,s}}{\partial z^2} \right), \quad (13)$$

where $(\rho c)_{i,s}$ is the volumetric heat capacity of the ice or snow, $T_{i,s}$ is the ice or snow temperature with depth (K), t is time (seconds), and $k_{i,s}$ is the thermal conductivity of ice or snow. As the heat capacity and thermal conductivity of the ice are affected by its temperature and salinity, the volumetric heat capacity of the sea ice ($\text{Jm}^{-3}\text{K}^{-1}$) is defined as (e.g. [2]),

$$(\rho c)_i = (\rho c)_{i,f} + \frac{\gamma S_i}{(T_i - 273)^2}, \quad (14)$$

where $(\rho c)_{i,f}$ is the volumetric heat capacity of pure ice ($1.883 \times 10^6 \text{ Jm}^{-3}\text{K}^{-1}$) and γ is a constant ($1.715 \times 10^7 \text{ JKm}^{-3}\text{ppt}^{-1}$), and S_i is the ice salinity (ppt).

The ice salinity was modelled as a function of the ice thickness according to (e.g. [6]),

$$\begin{aligned} S_i &= 13.4 - 17.4h_i, \quad h_i \leq 0.34 \text{ m}, \\ S_i &= 8.0 - 1.62h_i, \quad h_i > 0.34 \text{ m}, \end{aligned} \quad (15)$$

where h_i is the ice thickness. Although the ice salinity was directly measured during both field campaigns, the goal of demonstrating the use of the thermodynamic model for estimating depth-mean ice temperature is to show how the results are obtained when no in-situ field snow or ice measurements are available—hence, ice salinity is estimated from ice thickness which can also be remotely sensed or estimated. Based on the average field site ice thicknesses in 2017–2019 (64, 50, and 60.4 cm, respectively—see Table 1), average field site ice salinities of 6.96, 7.19, and 7.02 ppt are calculated from Equation (15) for 2017–2019, respectively. These values are within the range of ice salinities measured during the 2017–2019 field campaigns of 2–8 ppt.

The ice thermal conductivity ($\text{Wm}^{-1}\text{K}^{-1}$) is defined as (e.g. [2]),

$$k_i = k_{i,f} + \frac{BS_i}{T_i - 273}, \quad (16)$$

where $k_{i,f}$ is the thermal conductivity of pure ice ($2.034 \text{ W m}^{-1}\text{K}^{-1}$), and B is a constant ($0.1172 \text{ W m}^{-1}\text{ppt}^{-1}$). As per Ebert and Curry [2]; T_i is constrained to values 272.9 K or less in order to avoid a singularity at 273 K in Equations (14) and (16).

The volumetric heat capacity of the snow ($\text{Jm}^{-3}\text{K}^{-1}$) is defined as (e.g. [2]),

$$(\rho c)_s = \rho_s (92.88 + 7.364T_s), \quad (17)$$

where ρ_s is the snow density and T_s is the snow temperature (K). The snow density is assumed to be 330 kgm^{-3} when the air temperature is below 0°C (e.g., see [2]. The snow thermal conductivity ($\text{Wm}^{-1}\text{K}^{-1}$) is defined as (e.g. [2]),

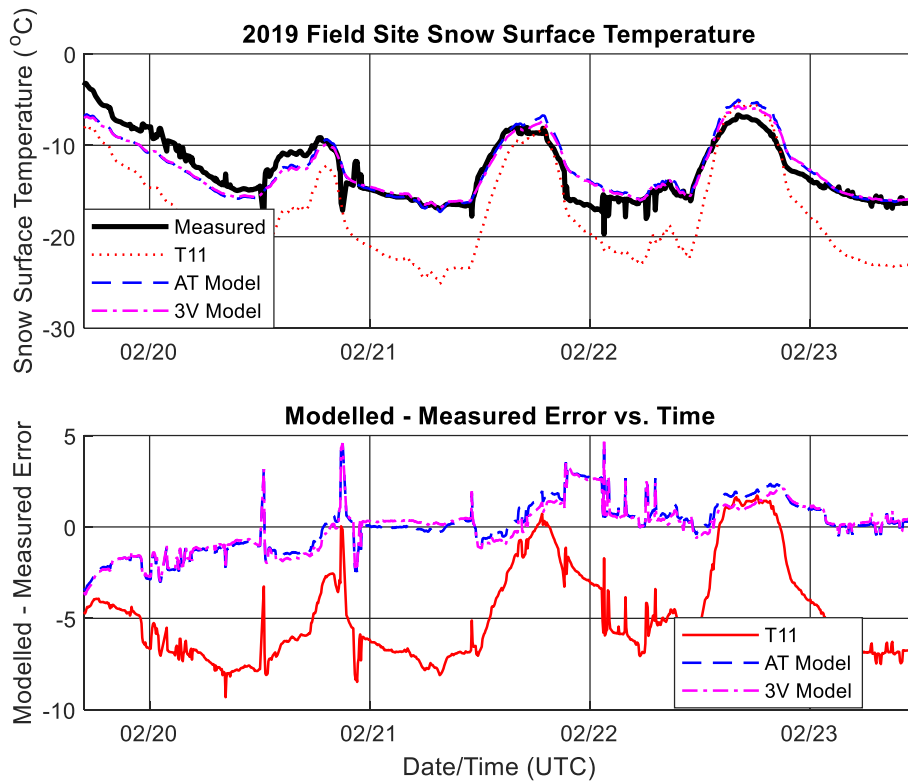


Fig. 14. Five-minute average measured and modelled snow surface temperatures during the 2019 campaign (top panel), and model errors (bottom panel).

$$k_s = (2.845 \times 10^{-6}) \rho_s^2 + (2.7 \times 10^{-4}) \left(2^{\frac{T_i - 233}{5}} \right). \quad (18)$$

Equation (13) is solved for the snow and ice temperature, $T_{i,s}$, using the standard Euler-forward scheme and centered finite-differencing for

second-order differential equations between the first and second time-steps, and the Dufort-Frankel algorithm (e.g., [2]; and [25] from the second time-step onward.

The Euler-forward scheme with centered finite-differencing for solution of the snow or ice temperature profile is represented by (e.g. [26],

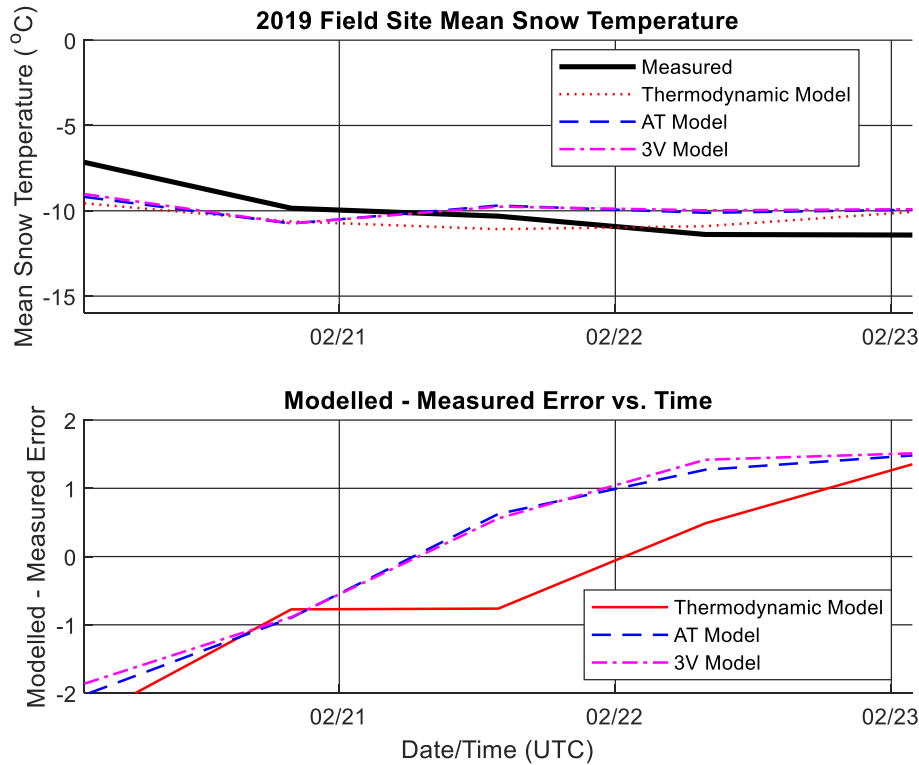


Fig. 15. Eighteen-hour average measured and modelled depth-mean snow temperatures during the 2019 campaign (top panel), and model errors (bottom panel).

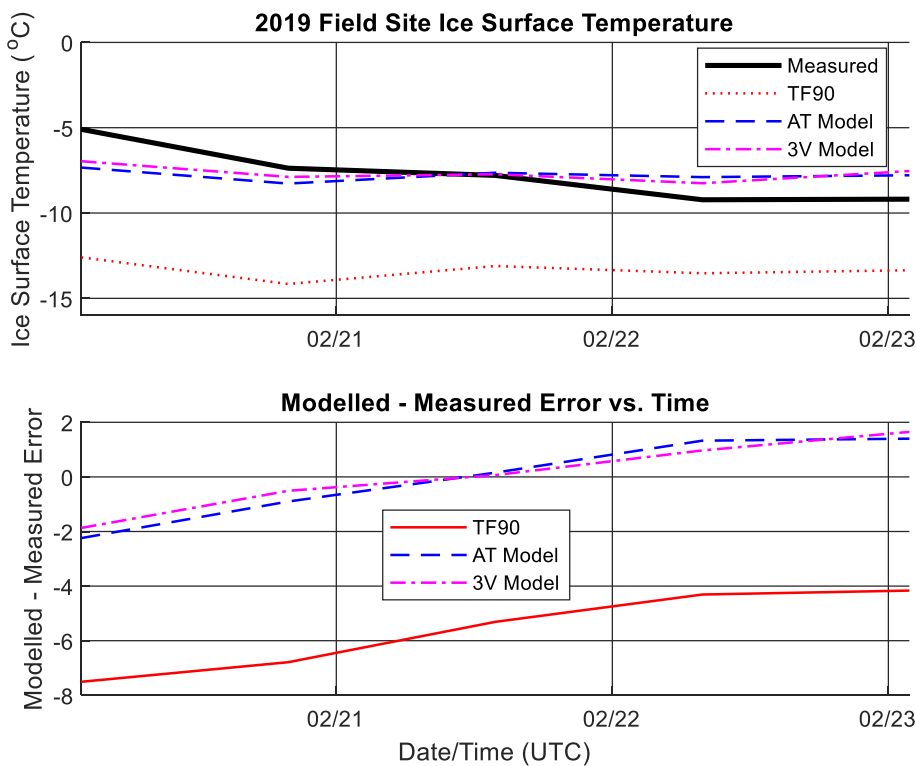


Fig. 16. Eighteen-hour average measured and modelled ice surface temperatures during the 2019 campaign (top panel), and model errors (bottom panel).

$$T_{i,s_{i+1}}^j = T_{i,s_i}^j + \frac{\kappa\Delta t}{\Delta z^2} (T_{i,s_i}^{j+1} - 2T_{i,s_i}^j + T_{i,s_i}^{j-1}) : i = 1, \quad (20)$$

where i is the time-step index, j is the depth level index in the snow or ice layer, κ is the quotient of the thermal conductivity and the volumetric heat capacity for snow or ice, Δt is the time-step (seconds) and Δz is the

spacing between depth levels (m). The Dufort-Frankel algorithm is represented by (e.g. [26]),

$$T_{i,s_{i+1}}^j = \left(\frac{1 - \beta}{1 + \beta} \right) T_{i,s_{i-1}}^j + \left(\frac{\beta}{1 + \beta} \right) (T_{i,s_i}^{j+1} + T_{i,s_i}^{j-1}) : i \geq 2, \quad (21)$$

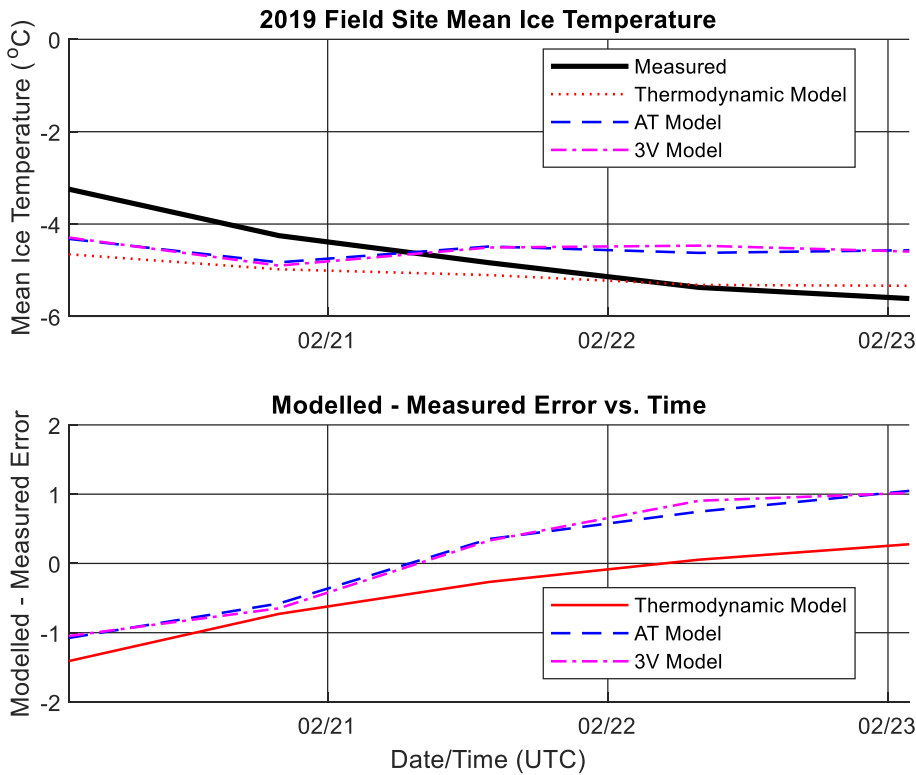


Fig. 17. Eighteen-hour average measured and modelled depth-mean ice temperatures during the 2019 campaign (top panel), and model errors (bottom panel).

where β represents the quantity $2 \frac{\kappa \Delta t}{\Delta z^2}$. The time-step Δt corresponds to the 18-h averaging time used to determine the optimal linear regression formulas for snow or ice depth-mean temperature (e.g., see Table 1).

The boundary conditions for the thermodynamic model are set using the 3 V formula for snow surface temperature, and the basal ice temperature was held constant at the TAC-measured freezing point of the seawater (approximately -1.8°C). The snow and ice temperature profiles are initialized in the thermodynamic model as linear from the snow surface to the ice base.

Fig. 14 shows the measured 5-min average snow surface temperatures versus time for the 2019 campaign, along with the modelled 5-min snow surface temperatures predicted from the T11 model and the new AT and 3 V models presented in this paper (top panel). Similar time-series plots for the 2017–2018 campaigns are shown in Figure 28 and Figure 29 in Appendix A. The bottom panel shows the modelled minus measured error for each snow surface temperature model versus time. While all three models simulate the snow surface temperature reasonably well for snow surface temperatures warmer than about -5°C , the AT and 3 V models perform significantly better than the T11 model for colder snow surface temperatures.

Fig. 15 shows the measured 18-h average snow depth-mean temperatures versus time for the 2019 campaigns, along with the modelled 18-h snow depth-mean temperatures predicted from the thermodynamic, AT, and 3 V models (top panel), and the modelled minus measured errors versus time (bottom panel). Similar time-series plots for the 2017–2018 campaigns are shown in Figure 30 and Figure 31 in Appendix A. While all three models generally simulate the trends in the snow depth-mean temperature versus time, the AT and 3 V models perform somewhat better than the thermodynamic model, particularly during February 22–23, 2017.

Fig. 16 shows the measured 18-h average ice surface temperatures versus time for the 2019 campaign, along with the modelled 18-h ice surface temperatures predicted from the TF90 model and the AT and 3 V models presented in this paper (top panel), and modelled minus measured model errors versus time (bottom panel). Similar time-series plots for the 2017–2018 campaigns are shown in Figure 32 and Figure 33 in Appendix A. While all three models generally simulate the trends in the ice surface temperature versus time, the AT and 3 V models perform significantly better than the TF90 model. The TF90 model tends to predict significantly colder ice surface temperatures than were observed during the three campaigns. In 2017–2018, the TF90 model tends to exaggerate the amplitude of the ice surface temperature changes in response to the surface air temperature.

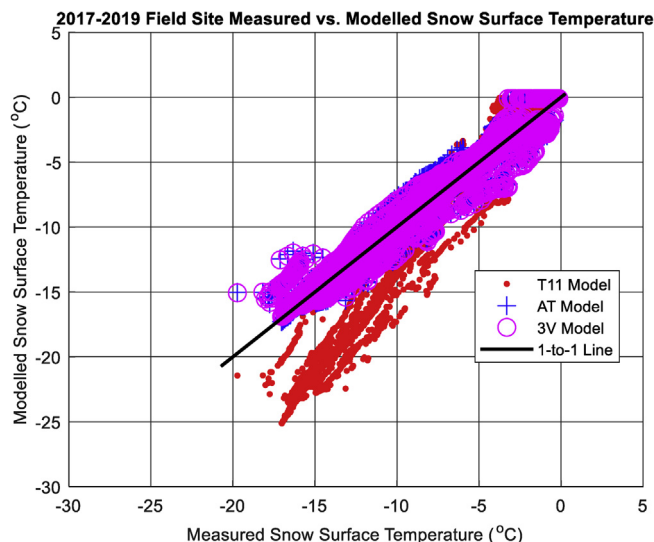


Fig. 18. Five-minute average measured vs. modelled snow surface temperature from the 2017–2019 campaigns.

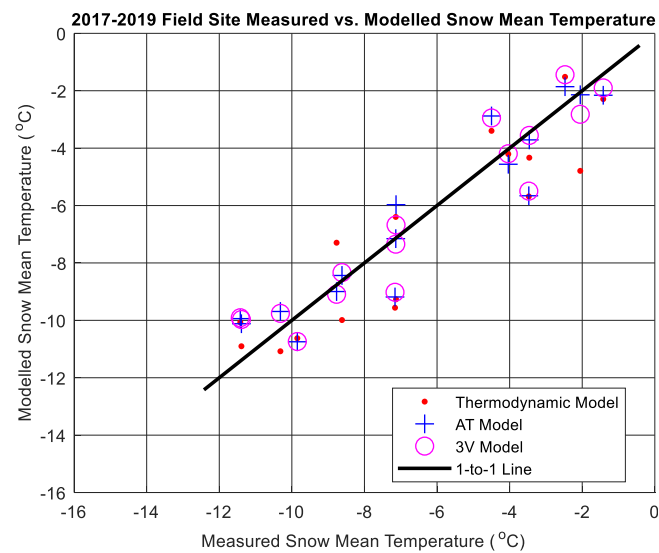


Fig. 19. Eighteen-hour average measured vs. modelled depth-mean snow temperature from the 2017–2019 campaigns.

Fig. 17 shows the measured 18-h average ice depth-mean temperatures versus time for the 2017–2019 campaigns, along with the modelled 18-h ice depth-mean temperatures predicted from the thermodynamic, AT, and 3 V models (top panel), and modelled minus measured model errors versus time (bottom panel). Similar time-series plots for the 2017–2018 campaigns are shown in Figure 34 and Figure 35 in Appendix A. The AT and 3 V models perform somewhat better than the thermodynamic model, however the difference between the thermodynamic and regression models are not as pronounced as they are for the snow depth-mean temperatures.

Table 7 in Appendix A summarizes statistics for the modelled minus measured errors from the snow and ice surface and depth-mean temperatures for the 2017–2019 field campaigns. The results in Table 7 show that on average, the 3 V model produces the smallest error relative to the observations for snow surface temperature, followed by the AT model, and the T11 model showing the largest errors relative to the observations. Similar results are apparent for ice surface temperatures, with the 3 V and AT models producing smaller errors compared to the TF90

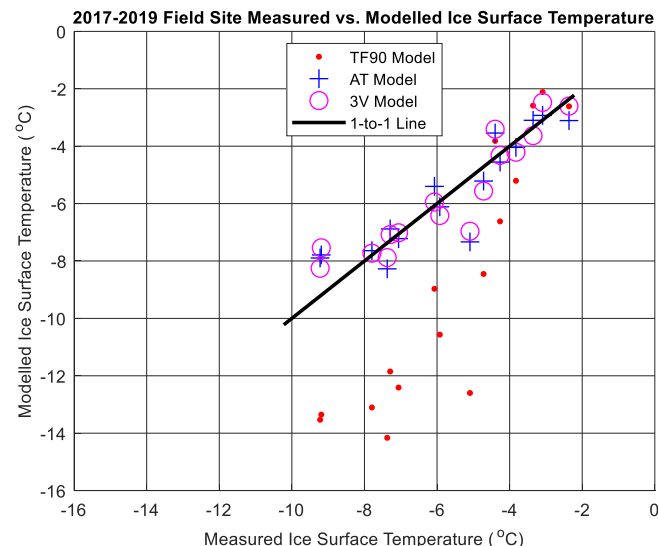


Fig. 20. Eighteen-hour average measured vs. modelled ice surface temperature from the 2017–2019 campaigns.

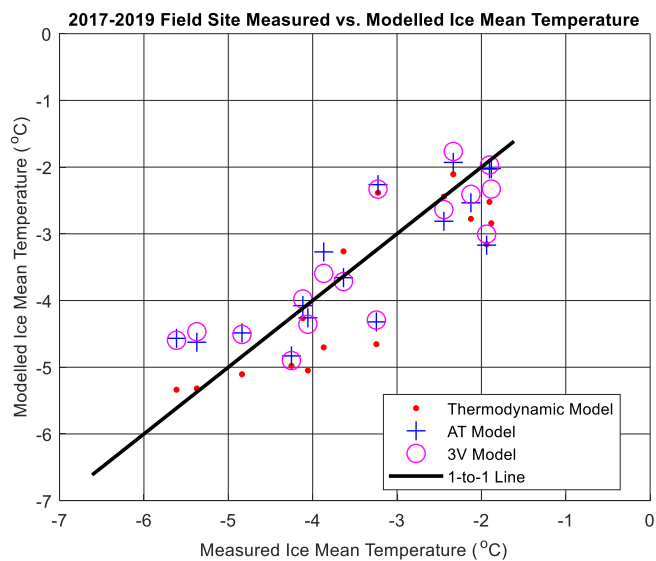


Fig. 21. Eighteen-hour average measured vs. modelled depth-mean ice temperature from the 2017–2019 campaigns.

model. However, for depth-mean snow and ice temperatures, the 3 V and AT models do not always outperform the one-dimensional thermodynamic model.

An informative way to assess the accuracy of the models described in this work for prediction of snow and ice surface and depth-mean temperature is to plot the measured versus modelled temperatures for the three field campaigns combined. Fig. 18 through Fig. 21 show the measured versus modelled 5-min average snow surface temperatures, 18-h depth-mean snow temperatures, ice surface temperatures, and depth-mean ice temperatures, respectively, for the 2017–2019 field campaigns and for all of the models previously discussed in this paper. The one-to-one line is shown in all four figures for reference.

Figs. 18 and Figure 20 show that the T11 and TF90 models are most accurate for prediction of snow and ice surface temperatures warmer than -5°C , respectively. Below -5°C , both the T11 and TF90 models tend to predict colder snow and ice surface temperatures than are observed. Figs. 19 and Figure 21 show that the thermodynamic model is not significantly less accurate for prediction of depth-mean snow and ice temperatures compared to the AT and 3 V regression models.

Conclusions

This paper offers simple linear models for the prediction of snow and sea ice surface and depth-mean temperatures as a function of readily obtainable surface meteorological variables. The models are robust, are simpler to implement than more complex thermodynamic energy balance models, and are more accurate overall than previous linear

regression models for snow and ice surface temperature. The robustness of the models is reinforced by the wide range of meteorological data on which they are based; e.g., between the three field campaigns, conditions ranged from calm to strong winds, cold to near-freezing air temperatures, and with a large range in atmospheric humidity levels. The models presented in this paper could have important applications for site-specific prediction of snow and sea ice temperatures, and by extension, temperature-dependent properties such as ice strength parameters. The meteorological variables on which the models depend can be remotely measured via satellites or in-situ automatic instrumentation left unmanned in the field, and are provided in many numerical weather forecast products. In addition, these models could be used for initialization of snow and ice temperature profiles in site-specific time-integrated thermodynamic energy balance models, as well as for definition of boundary conditions in these models.

While both the AT and 3 V models proved to be fairly robust for prediction of all four snow and ice temperature parameters, the 3 V models were more accurate. This result reinforces the important roles that atmospheric humidity and wind play in the energy balance of the snow and ice layers. However, use of air temperature alone is often adequate to obtain reasonably accurate estimates of snow and ice temperatures when averaged over the appropriate time periods for propagation of energy balance changes through the full depths of the snow and ice layers. This result is consistent with Turnbull and Taylor [27]; who found that the energy balance governing the break-up of land-fast ice offshore Labrador is predominantly controlled by the downwelling longwave radiation, which is in turn dependent upon primarily the air temperature and secondarily the humidity. However, Turnbull and Taylor [27] also found that the secondary contributors to the land-fast ice and snow energy balance, e.g., the solar radiation absorbed at the surface, and the sensible and latent heat fluxes (which are in turn both dependent on the wind speed and the latent heat flux is additionally dependent on the humidity), were very important in determining the timing of the onset of break-up.

Declaration of interests

The authors declare that they have no known competing financial interests or personal relationships that could have appeared to influence the work reported in this paper.

Acknowledgements

The authors gratefully acknowledge funding for this work by Hibernia Management and Development Company, Ltd. (HMDC), and InnovateNL. We additionally thank C-CORE for in-kind support of this work. We thank Soroosh Afzali, Marjan Taghi Boroojerdi, Ridwan Hossain, and Dr. Eleanor Bailey for their assistance with the field work. Finally, we thank Dr. Ricardo Vinuesa and Dr. Antonio García-Martínez for their very helpful comments which helped to improve the paper.

Appendix A

This section contains supplementary time-series plots of the field site measured air, snow surface, snow depth-mean, ice surface, and ice depth-mean temperatures, and wind speeds, for each of the 2017–2019 field campaigns, as well as for the NARR 2 m dew point temperatures used in the linear models. Also shown are a table of statistics for the field site meteorological variables, tables providing all linear models as a function of data time-averaging period, and a table of model error statistics.

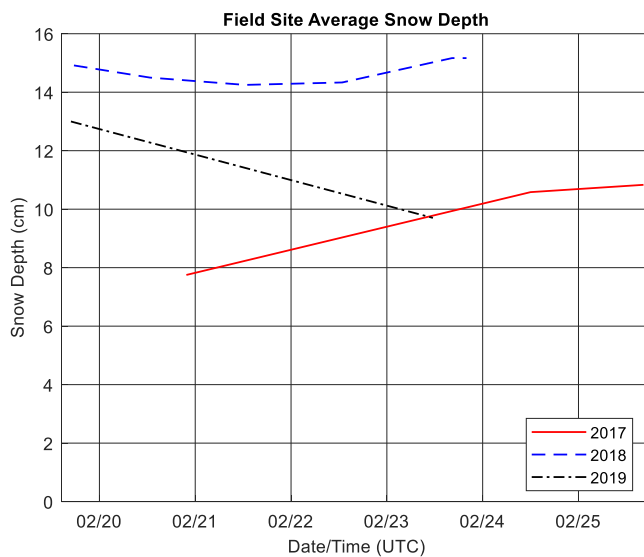


Fig. 22. Measured and interpolated average field site snow depths during the 2017–2019 campaigns.

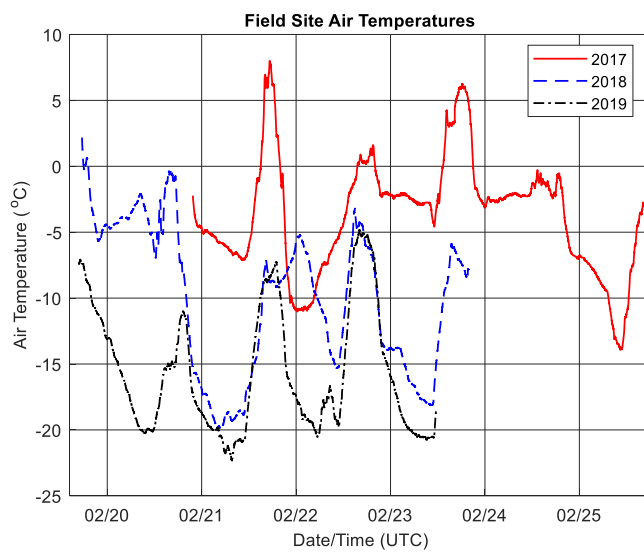


Fig. 23. Mean measured air temperatures at the field site during the 2017–2019 campaigns.

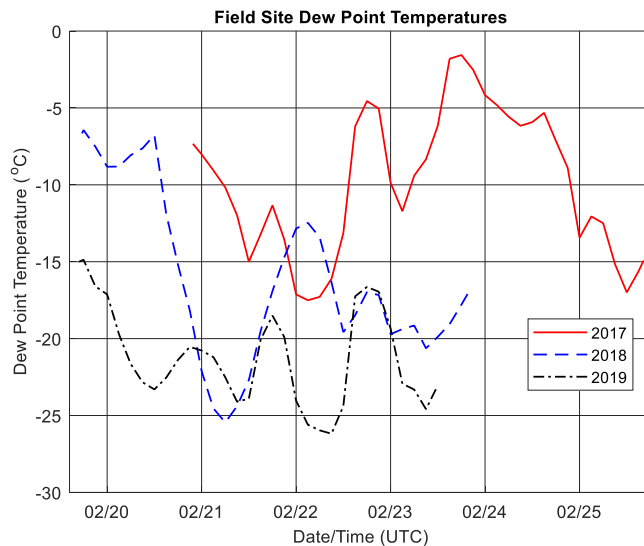


Fig. 24. Dew point temperatures (NARR) at the field site during the 2017–2019 campaigns.

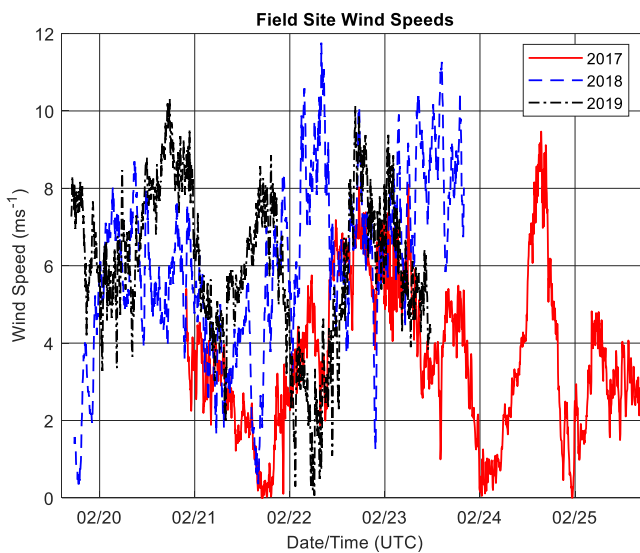


Fig. 25. Mean measured wind speeds at the field site during the 2017–2019 campaigns.

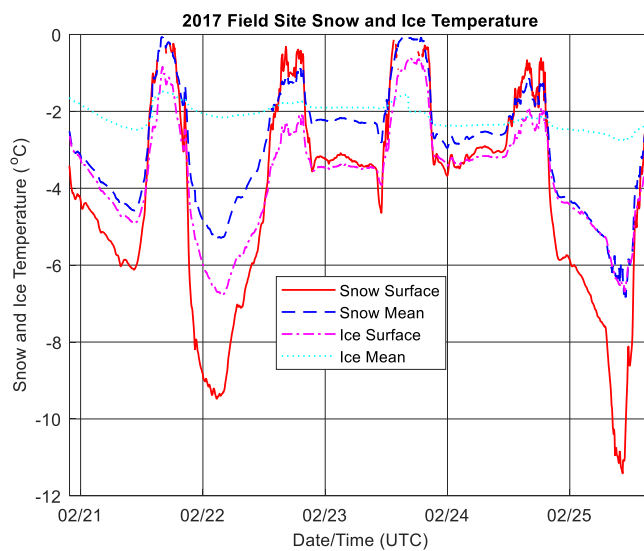


Fig. 26. Snow surface, depth-mean snow, ice surface, and depth-mean ice temperatures at the field site during the 2017 campaign.

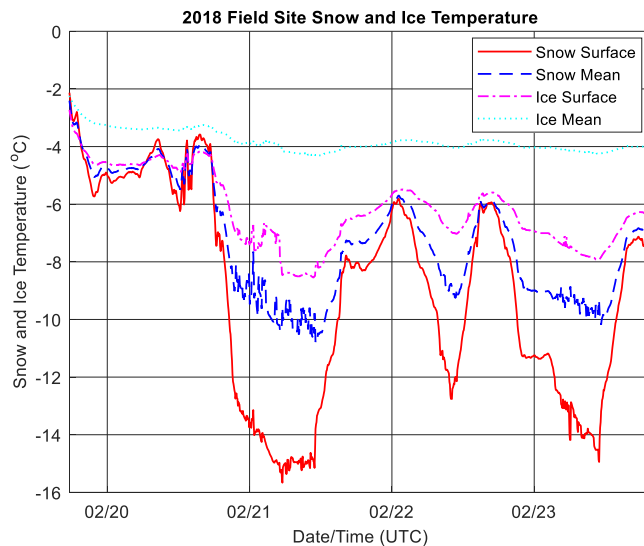


Fig. 27. Snow surface, depth-mean snow, ice surface, and depth-mean ice temperatures at the field site during the 2018 campaign.

Table 2

Summary statistics for all snow, ice, and meteorological variables during the 2017–2019 field campaigns.

Variable	Year	Mean	Minimum	Maximum	Standard Deviation
Air Temperature (°C)	2017	-3.71	-13.93	8.00	4.35
	2018	-9.98	-19.90	2.18	5.63
	2019	-15.62	-22.34	-4.75	4.71
Dew Point Temperature (°C)	2017	-9.82	-17.50	-1.57	4.54
	2018	-16.24	-25.44	-6.45	5.28
	2019	-21.33	-26.18	-14.88	2.89
Wind Speed (ms ⁻¹)	2017	3.66	0.00	9.47	1.98
	2018	6.02	0.35	11.76	2.22
	2019	6.04	0.06	10.30	1.99
Snow Surface Temperature (°C)	2017	-4.28	-11.42	-0.14	2.59
	2018	-9.02	-15.66	-2.13	3.61
	2019	-12.67	-19.73	-3.21	3.46
Snow Depth-Mean Temperature (°C)	2017	-2.91	-6.84	-0.07	1.54
	2018	-7.28	-10.78	-2.41	2.01
	2019	-10.05	-14.01	-2.61	2.32
Ice Surface Temperature (°C)	2017	-3.67	-6.76	-0.58	1.43
	2018	-6.20	-8.55	-2.73	1.28
	2019	-7.76	-11.72	-2.18	1.82
Ice Depth-Mean Temperature (°C)	2017	-2.13	-2.77	-1.48	0.30
	2018	-3.80	-4.32	-2.24	0.37
	2019	-4.68	-6.12	-1.79	0.91
Snow Thickness (cm)	2017	9.55	7.75	10.83	0.97
	2018	14.55	14.25	15.17	0.27
	2019	11.35	9.70	13.00	0.95
Ice Thickness (cm)	2017	64.0	63.0	65.0	1.0
	2018	50.0	48.0	52.0	2.0
	2019	60.4	58.0	62.5	1.9

Table 3Variable averaging periods, R² values, and slopes and intercepts for AT and 3V snow surface temperature linear regression models.

Averaging Period (Minutes)	AT Model			3 V Model				
	R ² Value	T _a Slope	Intercept	R ² Value	T _a Slope	T _d Slope	W _s Slope	Intercept
5	0.95	0.701711329	-1.642883496	0.96	0.608248598	0.10748242	-0.023994102	-0.745952046
10	0.95	0.701353913	-1.64768062	0.96	0.607832872	0.107434944	-0.02423459	-0.751629098
15	0.95	0.701315959	-1.644402654	0.96	0.607972116	0.107384615	-0.023736658	-0.749597652
20	0.95	0.701538446	-1.646877727	0.96	0.606872122	0.108574352	-0.023511429	-0.748837495
30	0.95	0.701505554	-1.641960104	0.96	0.608615634	0.106376634	-0.02538327	-0.751361412
60	0.96	0.701246437	-1.63539016	0.96	0.604814207	0.109965994	-0.023494977	-0.73434475
120	0.96	0.703577359	-1.602092905	0.96	0.603291502	0.112568539	-0.027313999	-0.681421753
180	0.96	0.711887928	-1.482982041	0.97	0.602559123	0.118719457	-0.038000227	-0.511909604
240	0.96	0.717737502	-1.409946555	0.97	0.604718683	0.1202186	-0.054270275	-0.368642515
300	0.96	0.718843565	-1.382521947	0.97	0.598757637	0.125774042	-0.059674775	-0.30346709
360	0.96	0.723889929	-1.304550979	0.97	0.596298796	0.127163662	-0.071281959	-0.222396564
420	0.96	0.730768258	-1.242807862	0.97	0.595895884	0.131729968	-0.080224703	-0.106570452
480	0.96	0.727954169	-1.29756998	0.97	0.573152111	0.148564018	-0.064284431	-0.182746749
540	0.96	0.730989592	-1.192493649	0.97	0.576104293	0.149875156	-0.056946641	-0.129827451
600	0.96	0.731980659	-1.160516996	0.97	0.583186711	0.140393615	-0.065709752	-0.144549151
660	0.96	0.726913584	-1.217065346	0.97	0.584857222	0.137183849	-0.059860622	-0.20863588
720	0.96	0.747676956	-1.069012416	0.96	0.551519506	0.170126381	-0.070348062	0.01384408
780	0.96	0.735189665	-1.172932539	0.97	0.587848938	0.136326685	-0.043943637	-0.285775769
840	0.96	0.73926365	-1.135578277	0.97	0.599916403	0.119731729	-0.102315131	-0.121729185
900	0.96	0.731848458	-1.147170514	0.97	0.570563456	0.143802302	-0.107972673	0.015835896
960	0.95	0.738909203	-1.099968157	0.96	0.491224225	0.216330694	-0.064579269	0.138103745
1020	0.96	0.745933995	-1.044511676	0.97	0.494480077	0.218219521	-0.034683468	0.028514503
1080	0.97	0.750261336	-0.994149579	0.97	0.533021915	0.184703529	-0.066914193	0.032190677
1140	0.97	0.745994435	-1.032651557	0.98	0.463887206	0.228782333	-0.132867954	0.435352319
1200	0.96	0.742497399	-1.107874056	0.97	0.490045576	0.212170951	-0.071019648	0.088052318
1260	0.97	0.744275868	-1.089254444	0.97	0.504122593	0.200241684	-0.085317023	0.094276924
1320	0.97	0.741944747	-1.081388034	0.97	0.490322629	0.205015699	-0.13426801	0.268950135
1380	0.97	0.728124393	-1.14375537	0.97	0.378962761	0.299552784	-0.14832901	0.772671571
1440	0.96	0.731680084	-1.14842448	0.97	0.273810852	0.398045678	-0.132281009	1.201772884

Table 4Variable averaging periods, R^2 values, and slopes and intercepts for AT and 3V snow depth-mean temperature linear regression models.

Averaging Period (Minutes)	AT Model			3 V Model				
	R^2 Value	T _a Slope	Intercept	R^2 Value	T _a Slope	T _d Slope	W _s Slope	Intercept
5	0.84	0.485036193	-1.926588556	0.88	0.318096557	0.186787753	-0.134899511	0.073119027
10	0.84	0.48464815	-1.930966803	0.88	0.317504785	0.186659806	-0.135005983	0.063870606
15	0.84	0.485191639	-1.924079811	0.88	0.319141223	0.185336241	-0.137328456	0.072949385
20	0.84	0.484816585	-1.929230583	0.88	0.317124483	0.186724651	-0.135302033	0.060909389
30	0.84	0.485262617	-1.919698307	0.88	0.319385045	0.18420132	-0.139596978	0.07043339
60	0.84	0.485972596	-1.907475076	0.88	0.318779628	0.183762347	-0.144995951	0.087912436
120	0.85	0.489137102	-1.867536334	0.88	0.319026143	0.183711903	-0.155053942	0.145074709
180	0.85	0.499528558	-1.718284863	0.89	0.320286149	0.18721931	-0.166479642	0.294586305
240	0.85	0.503931417	-1.642380287	0.89	0.320988801	0.187142305	-0.185450333	0.429765918
300	0.85	0.511273643	-1.572992712	0.89	0.328984464	0.182772988	-0.19755221	0.487970909
360	0.86	0.523019424	-1.411326974	0.90	0.315781053	0.198369025	-0.214933077	0.728229711
420	0.85	0.515594914	-1.47443843	0.89	0.298879473	0.204153945	-0.221812442	0.715895433
480	0.87	0.533459671	-1.326976871	0.90	0.323075035	0.190210772	-0.210972621	0.643547825
540	0.86	0.532200591	-1.275701555	0.89	0.282380974	0.230306496	-0.226847926	0.950731236
600	0.86	0.540972486	-1.166837322	0.89	0.318402068	0.197189323	-0.244207295	0.897373555
660	0.86	0.53656319	-1.212296159	0.90	0.310619343	0.203723293	-0.249546883	0.951386427
720	0.87	0.56386325	-1.000516613	0.90	0.319141595	0.198918939	-0.203927323	0.736892993
780	0.87	0.538427368	-1.195281975	0.90	0.282221873	0.21870355	-0.241029324	0.909495613
840	0.85	0.550283414	-1.09898144	0.89	0.300448202	0.208494724	-0.239320378	0.91300684
900	0.86	0.555791097	-1.024669109	0.90	0.303501122	0.207639742	-0.305831388	1.230442739
960	0.85	0.56518058	-0.903558581	0.89	0.255536232	0.250142831	-0.270765352	1.307874214
1020	0.88	0.587547483	-0.738288489	0.89	0.386954528	0.153563479	-0.219703813	0.780781627
1080	0.89	0.59979569	-0.589880619	0.90	0.367222696	0.180291646	-0.199473069	0.893426051
1140	0.87	0.578706797	-0.763697155	0.91	0.194930449	0.295531335	-0.289204547	1.545392095
1200	0.87	0.576583106	-0.878523414	0.90	0.253554396	0.236656079	-0.334449139	1.355058146
1260	0.87	0.578047122	-0.861504002	0.90	0.274185542	0.212739406	-0.381311994	1.40504351
1320	0.88	0.580194804	-0.782533119	0.90	0.267644984	0.226932397	-0.355227894	1.426224652
1380	0.89	0.551353923	-0.948720941	0.90	0.140747687	0.342822936	-0.254086181	1.570709986
1440	0.88	0.557012524	-0.971781466	0.92	-0.07461153	0.538086366	-0.270462305	2.559383531

Table 5Variable averaging periods, R^2 values, and slopes and intercepts for AT and 3V ice surface temperature linear regression models.

Averaging Period (Minutes)	AT Model			3 V Model				
	R^2 Value	T _a Slope	Intercept	R^2 Value	T _a Slope	T _d Slope	W _s Slope	Intercept
5	0.64	0.263546814	-3.309588998	0.74	0.063949628	0.228786389	-0.067123527	-1.324043799
10	0.64	0.263386235	-3.310305644	0.74	0.063280207	0.229033994	-0.067314464	-1.32621023
15	0.64	0.264056391	-3.302152794	0.75	0.065632668	0.227166559	-0.069834595	-1.316982369
20	0.64	0.2638386	-3.304252904	0.75	0.062903201	0.229433039	-0.067708237	-1.321849725
30	0.65	0.264166087	-3.295648085	0.75	0.064943988	0.227150585	-0.071253555	-1.314044827
60	0.65	0.265175461	-3.277732187	0.76	0.064893133	0.226588256	-0.076054506	-1.293085839
120	0.66	0.267759062	-3.243633712	0.77	0.05982798	0.231939795	-0.078546181	-1.24383867
180	0.67	0.277720388	-3.100372281	0.78	0.056786619	0.239111113	-0.088018044	-1.09266254
240	0.68	0.281883943	-3.02904631	0.79	0.058488356	0.237547766	-0.108307169	-0.966680192
300	0.69	0.286305096	-2.991421379	0.79	0.063239756	0.23362812	-0.110890265	-0.986861303
360	0.69	0.296681811	-2.843843866	0.81	0.030016367	0.267604482	-0.126753589	-0.667740897
420	0.68	0.294131045	-2.865481499	0.80	0.018064384	0.27344235	-0.117117619	-0.724559361
480	0.73	0.310422474	-2.71994749	0.82	0.030386909	0.269063107	-0.112991584	-0.715394682
540	0.71	0.304138104	-2.732676152	0.83	-0.034245323	0.327601044	-0.122483185	-0.418358049
600	0.71	0.307622802	-2.690746225	0.82	-0.009420358	0.30065833	-0.12277077	-0.59030341
660	0.71	0.30141107	-2.74892747	0.82	0.008702803	0.280423288	-0.147288684	-0.584204948
720	0.76	0.33319909	-2.475971844	0.82	-0.001601909	0.29626236	-0.083892324	-0.739823547
780	0.75	0.30985974	-2.640231922	0.85	-0.020501657	0.302563904	-0.126358834	-0.55605444
840	0.72	0.316282936	-2.628808973	0.83	-0.076943608	0.360903309	-0.080211331	-0.492688913
900	0.75	0.320175595	-2.558487107	0.85	-0.007838631	0.304712716	-0.122611177	-0.501908979
960	0.75	0.327779873	-2.477890878	0.86	-0.096636155	0.372153856	-0.096952881	-0.404280562
1020	0.80	0.349175675	-2.284973396	0.84	-0.058704889	0.351361699	-0.080685509	-0.460089606
1080	0.82	0.360734798	-2.16519128	0.85	0.027177449	0.290194751	-0.054431573	-0.734627675
1140	0.77	0.339344821	-2.345684261	0.87	-0.126455604	0.39685129	-0.087478171	-0.301303853
1200	0.72	0.334242383	-2.437664819	0.84	-0.13798417	0.400298317	-0.108932925	-0.269661496
1260	0.72	0.333953327	-2.450206495	0.84	-0.165218184	0.412353413	-0.203309073	0.082896924
1320	0.75	0.336402954	-2.406450551	0.84	-0.170279154	0.421434561	-0.211903362	0.147790132
1380	0.80	0.317392617	-2.459907666	0.88	-0.250326432	0.49834914	-0.145941917	0.338372388
1440	0.80	0.32444659	-2.452840838	0.90	-0.34908775	0.591832915	-0.144251296	0.838943444

Table 6

Variable averaging periods, R^2 values, and slopes and intercepts for AT and 3V ice depth-mean temperature linear regression models.

Averaging Period (Minutes)	AT Model			3 V Model				
	R^2 Value	T _a Slope	Intercept	R^2 Value	T _a Slope	T _d Slope	W _s Slope	Intercept
5	0.52	0.133473945	-2.188915951	0.63	0.042617582	0.100124665	-0.099882428	-0.9866628
10	0.52	0.133314039	-2.190287384	0.63	0.042395166	0.09994528	-0.100381285	-0.989730379
15	0.52	0.133691012	-2.185660495	0.63	0.043279176	0.099286774	-0.101676418	-0.983809818
20	0.52	0.133471471	-2.188306144	0.63	0.042541637	0.099558341	-0.101428184	-0.989609729
30	0.52	0.133651536	-2.183695824	0.63	0.043290644	0.098647521	-0.103643143	-0.982615165
60	0.52	0.133828372	-2.178736901	0.63	0.043081474	0.097850715	-0.10726944	-0.977005711
120	0.53	0.135089896	-2.164622837	0.64	0.044454813	0.095894736	-0.112476196	-0.96842679
180	0.55	0.139012059	-2.108906716	0.65	0.046833288	0.094036531	-0.117133629	-0.946435819
240	0.55	0.140199968	-2.081987924	0.66	0.045228377	0.094992697	-0.124542799	-0.894296288
300	0.57	0.145373392	-2.034383761	0.67	0.04927599	0.094710016	-0.125698328	-0.862673216
360	0.58	0.150169084	-1.97783712	0.68	0.054195342	0.089089252	-0.133219516	-0.857268114
420	0.56	0.145542781	-2.012214739	0.67	0.041691886	0.095326834	-0.137267843	-0.84103981
480	0.61	0.156285384	-1.920103924	0.68	0.062444878	0.081179415	-0.132810995	-0.89854882
540	0.60	0.155851343	-1.91282114	0.69	0.038776526	0.104836566	-0.142841304	-0.730763067
600	0.61	0.160928752	-1.851912815	0.69	0.06209513	0.084102987	-0.147836829	-0.788283177
660	0.59	0.155660844	-1.901512974	0.68	0.039757605	0.102058882	-0.154096604	-0.696993035
720	0.63	0.169469573	-1.784651241	0.68	0.060502863	0.084543681	-0.123383043	-0.90402999
780	0.60	0.154643668	-1.901315083	0.68	0.025812622	0.107229623	-0.145814751	-0.758888039
840	0.60	0.164762207	-1.816526242	0.68	0.040687036	0.102146473	-0.131509286	-0.773318711
900	0.64	0.170216456	-1.772735545	0.70	0.049408728	0.099590927	-0.145150005	-0.697011597
960	0.61	0.170046281	-1.739804811	0.70	0.034076185	0.106025796	-0.154614676	-0.643991463
1020	0.67	0.185478168	-1.635121629	0.71	0.10704933	0.054455379	-0.138178833	-0.860677755
1080	0.71	0.195704265	-1.516003608	0.73	0.119447358	0.053052431	-0.109817849	-0.896056841
1140	0.64	0.17762526	-1.653500002	0.71	-0.000518427	0.134640209	-0.151797377	-0.531151762
1200	0.63	0.178581964	-1.709900957	0.68	0.04669314	0.091700319	-0.170982834	-0.698536848
1260	0.64	0.180435157	-1.687741754	0.69	0.062306968	0.073544135	-0.209875791	-0.633200145
1320	0.65	0.182068358	-1.644272036	0.69	0.04596352	0.090328836	-0.21241225	-0.519647718
1380	0.67	0.161446136	-1.769836062	0.71	-0.025306091	0.153736402	-0.134005339	-0.562418699
1440	0.66	0.165024422	-1.779269325	0.75	-0.147142539	0.26431812	-0.146612077	0.008460235

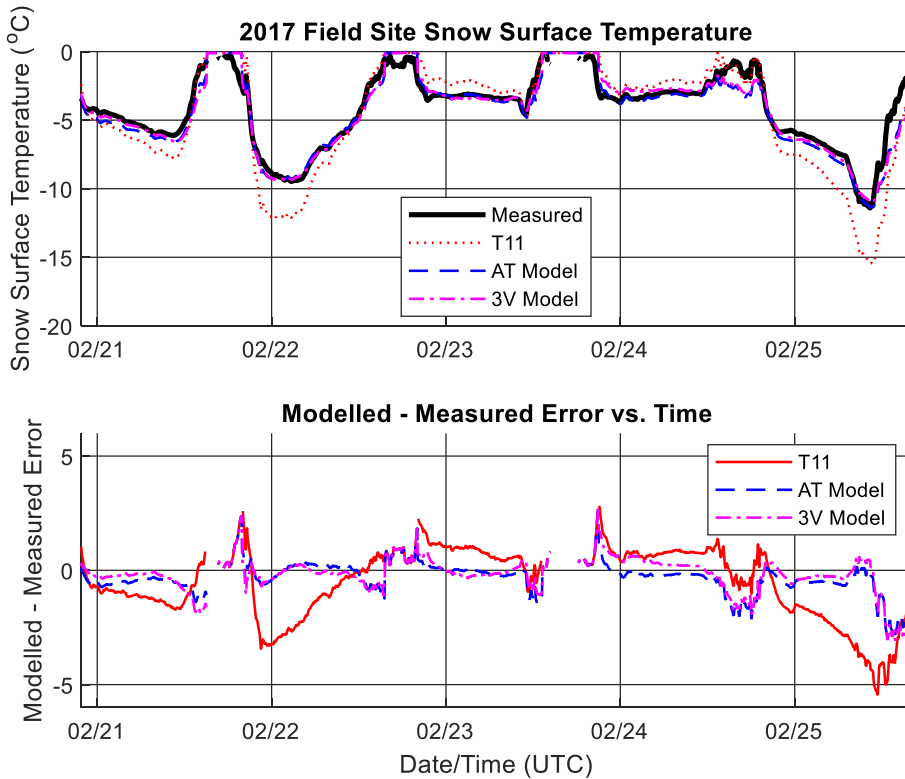


Fig. 28. Five-minute average measured and modelled snow surface temperatures during the 2017 campaign (top panel), and model errors (bottom panel).

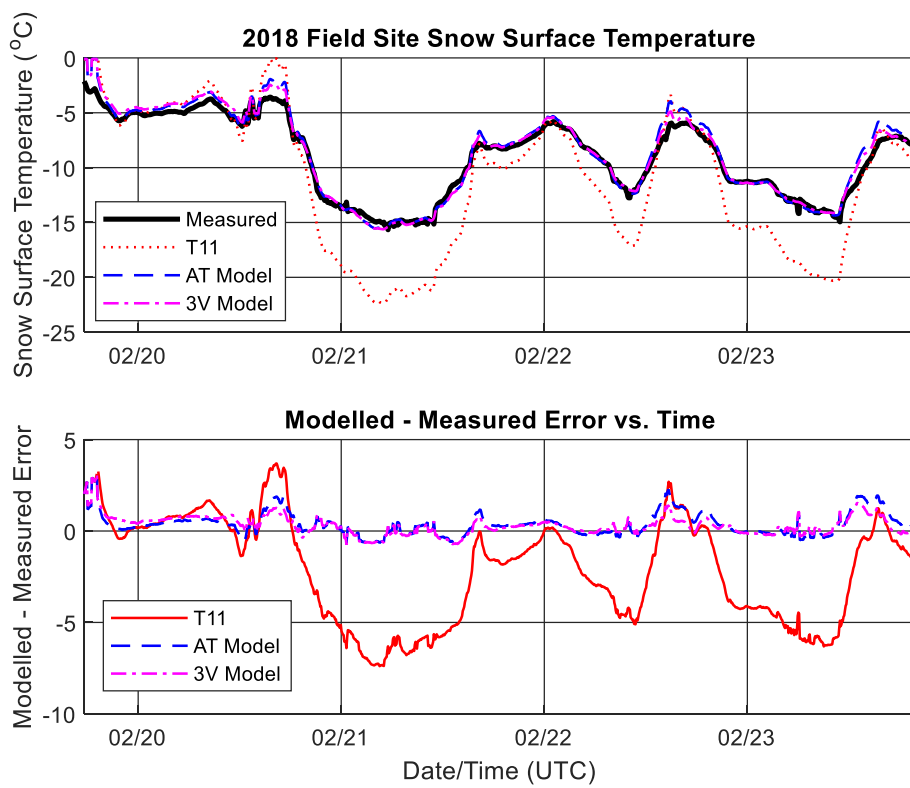


Fig. 29. Five-minute average measured and modelled snow surface temperatures during the 2018 campaign (top panel), and model errors (bottom panel).

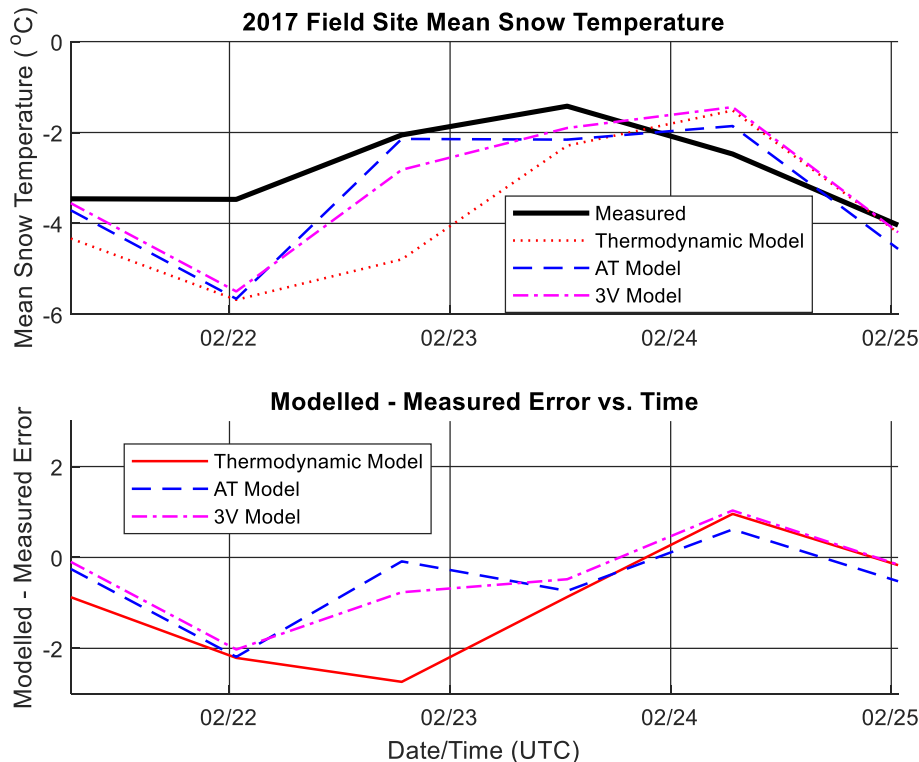


Fig. 30. Eighteen-hour average measured and modelled depth-mean snow temperatures during the 2017 campaign (top panel), and model errors (bottom panel).

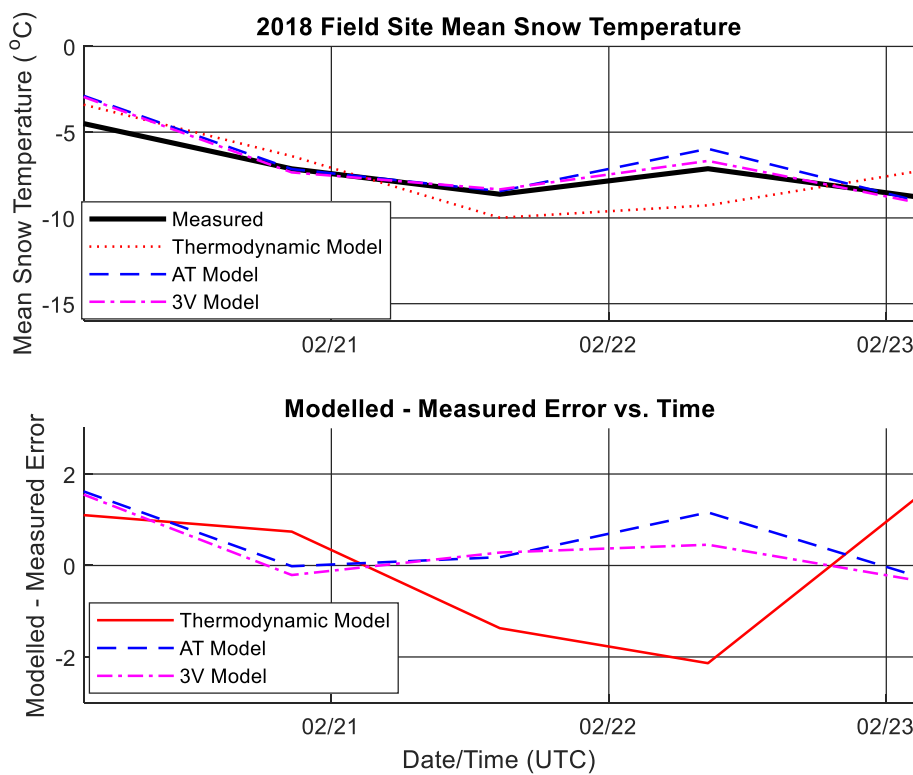


Fig. 31. Eighteen-hour average measured and modelled depth-mean snow temperatures during the 2018 campaign (top panel), and model errors (bottom panel).

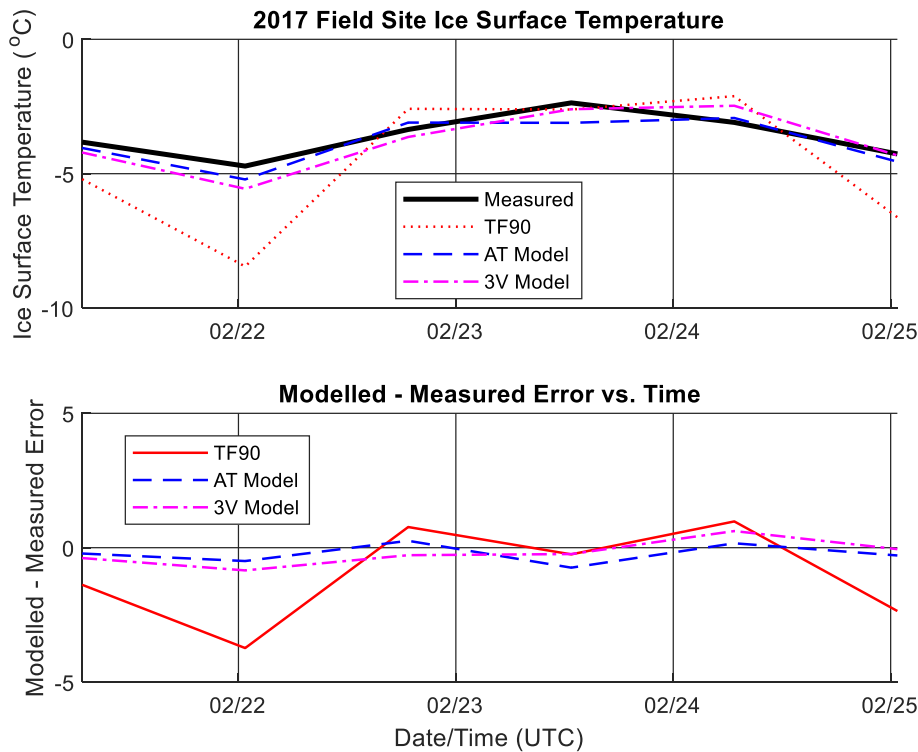


Fig. 32. Eighteen-hour average measured and modelled ice surface temperatures during the 2017 campaign (top panel), and model errors (bottom panel).

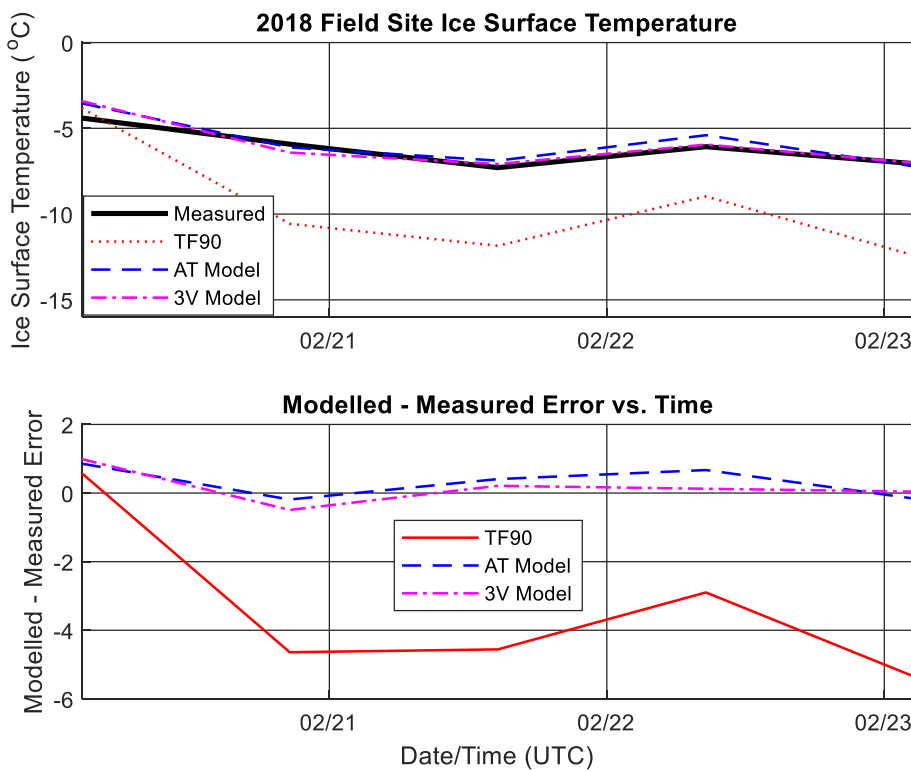


Fig. 33. Eighteen-hour average measured and modelled ice surface temperatures during the 2018 campaign (top panel), and model errors (bottom panel).

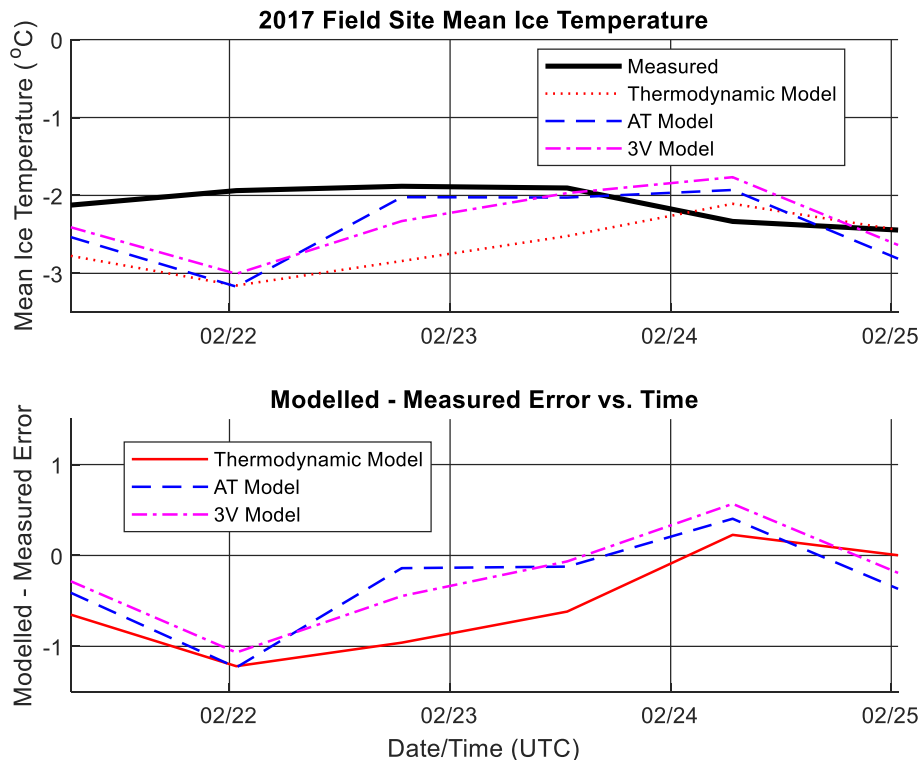


Fig. 34. Eighteen-hour average measured and modelled depth-mean ice temperatures during the 2017 campaign (top panel), and model errors (bottom panel).

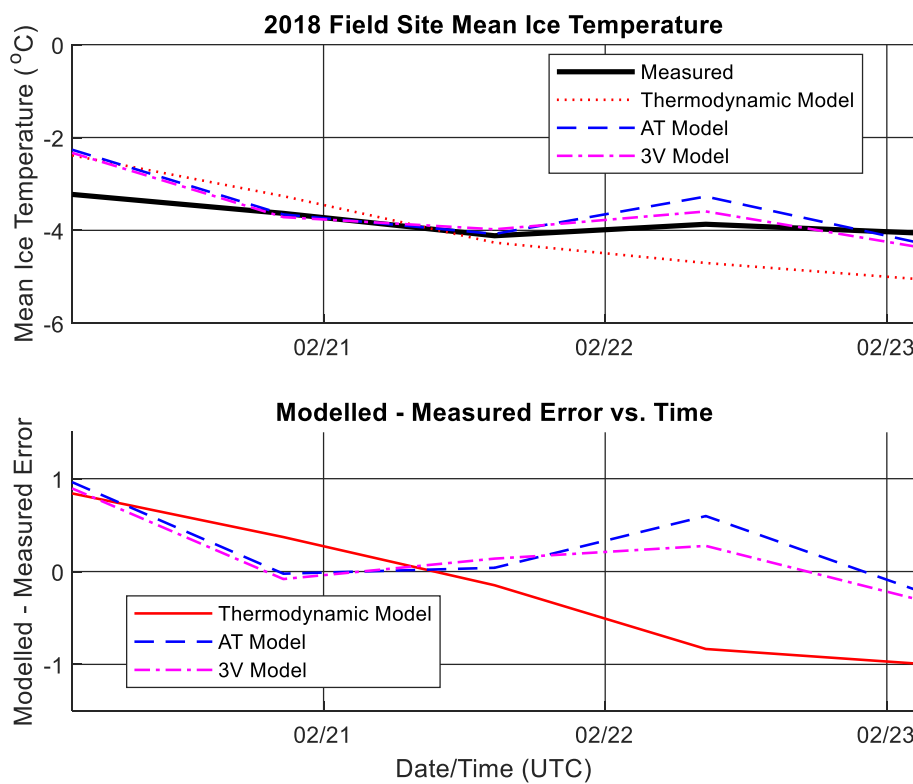


Fig. 35. Eighteen-hour average measured and modelled depth-mean ice temperatures during the 2018 campaign (top panel), and model errors (bottom panel).

Table 7

Summary statistics for modelled minus measured errors ($^{\circ}\text{C}$) for snow and ice surface and depth-mean temperature models.

Model		Year	Mean	Minimum	Maximum	Standard Deviation
Snow Surface Temperature	T11	2017	-0.52	-5.44	2.82	1.55
		2018	-2.11	-7.39	3.69	2.84
		2019	-4.81	-9.31	1.72	2.64
	AT	2017	-0.31	-2.93	2.69	0.70
		2018	0.38	-0.72	3.12	0.63
		2019	0.08	-3.48	4.70	1.39
	3V	2017	-0.19	-3.07	2.69	0.77
		2018	0.32	-0.75	3.12	0.52
		2019	0.00	-3.70	4.66	1.33
Snow Mean Temperature	Thermodynamic	2017	-0.98	-2.74	0.96	1.34
		2018	-0.04	-2.14	1.47	1.61
		2019	-0.42	-2.40	1.35	1.43
	AT	2017	-0.53	-2.19	0.62	0.94
		2018	0.54	-0.23	1.62	0.80
		2019	0.09	-2.03	1.48	1.51
	3V	2017	-0.42	-2.03	1.03	1.00
		2018	0.35	-0.32	1.55	0.75
		2019	0.15	-1.86	1.51	1.48
Ice Surface Temperature	TF90	2017	-1.00	-3.73	0.98	1.85
		2018	-3.37	-5.35	0.58	2.39
		2019	-5.62	-7.51	-4.16	1.49
	AT	2017	-0.22	-0.74	0.26	0.38
		2018	0.32	-0.19	0.86	0.48
		2019	-0.05	-2.24	1.40	1.55
	3V	2017	-0.20	-0.84	0.62	0.48
		2018	0.18	-0.49	0.99	0.53
		2019	0.06	-1.87	1.65	1.36
Ice Mean Temperature	Thermodynamic	2017	-0.54	-1.22	0.23	0.55
		2018	-0.15	-0.99	0.84	0.78
		2019	-0.42	-1.41	0.28	0.67
	AT	2017	-0.31	-1.23	0.40	0.54
		2018	0.28	-0.20	0.96	0.49
		2019	0.10	-1.08	1.05	0.90
	3V	2017	-0.25	-1.07	0.57	0.53
		2018	0.19	-0.30	0.90	0.45
		2019	0.11	-1.05	1.02	0.92

References

- [1] G.A. Maykut, N. Untersteiner, Some results from a time-dependent thermodynamic model of sea ice, *J. Geophys. Res.* 76 (6) (1971) 1,550–551,575.
- [2] E.E. Ebert, J.A. Curry, An intermediate one-dimensional thermodynamic sea ice model for investigating ice-atmosphere interactions, *J. Geophys. Res.* 98 (C6) (1993) 10,085–10,109.
- [3] North American Regional Reanalysis (NARR), NCEP Reanalysis Data provided by the NOAA/OAR/ESRL PSD, Boulder, Colorado, USA, 2019, from their Web site at, <http://www.esrl.noaa.gov/psd/>. (Accessed 10 April 2019).
- [4] D. Marks, J. Dozier, A clear-sky longwave radiation model for remote alpine areas, *Arch. Met. Geoph. Biokl. Ser. B* 27 (1979) 159–187.
- [5] M. Bjerkås, P.O. Moslet, P. Jochmann, S. Løset, Global ice loads on the lighthouse Norstrømsgaard in the winter 2001, in: Proceedings of the 17th International Conference on Port and Ocean Engineering under Arctic Conditions (POAC), Trondheim, Norway, June 16–19, 2003, pp. 935–941.
- [6] G.W. Timco, R.M.W. Frederking, Compressive strength of sea ice sheets, *Cold Reg. Sci. Technol.* 17 (1990) 227–240.
- [7] G.W. Timco, W.F. Weeks, A review of the engineering properties of sea ice, *Cold Reg. Sci. Technol.* 60 (2010) 107–129.
- [8] G.W. Timco, S. O'Brien, Flexural strength equation for sea ice, *Cold Reg. Sci. Technol.* 22 (1994) 285–298.
- [9] G.F.N. Cox, W.F. Weeks, Equations for determining the gas and brine volumes in sea ice samples, *J. Glaciol.* 29 (102) (1983) 306–316.
- [10] F. Schenk, R. Vinuesa, Enhanced large-scale atmospheric flow interaction with ice sheets at high model resolution, *Results in Engineering* 3 (2019). Article 100030.
- [11] S. Li, X. Zhou, K. Morris, Measurement of snow and sea ice surface temperature and emissivity in the Ross Sea, in: Proceedings of the 1999 International Geoscience and Remote Sensing Symposium (IGARSS), June 28–July 2, Hamburg, Germany, 1999, pp. 1034–1036.
- [12] S.G. Warren, I.G. Rigor, N. Untersteiner, V.F. Radionov, N.N. Bryazgin, Y.I. Aleksandrov, R. Colony, Snow depth on Arctic sea ice, *J. Clim.* 12 (1999) 1,814–1,829.
- [13] D.C. Powell, T. Markus, D.J. Cavalieri, A.J. Gasiewski, M. Klein, J.A. Maslanik, J.C. Stroeve, M. Sturm, Microwave signatures of snow on sea ice: modeling, *IEEE Trans. Geosci. Remote Sens.* 44 (11) (2006) 3,091–3,102.
- [14] M. Sturm, J.A. Maslanik, D.K. Perovich, J.C. Stroeve, J. Richter-Menge, T. Markus, J. Holmgren, J.F. Heinrichs, K. Tape, Snow depth and ice thickness measurements from the Beaufort and Chukchi seas collected during the AMSR-ice 03 campaign, *IEEE Trans. Geosci. Remote Sens.* 44 (11) (2006) 3,009–3,020.
- [15] C. Haas, M. Nicolaus, S. Willmes, A. Worby, D. Flinspach, Sea ice and snow thickness and physical properties of an ice floe in the western Weddell Sea and their changes during spring warming, *Deep-Sea Research II* 55 (2008) 963–974.
- [16] O. Lecomte, T. Fichefet, M. Vancoppenolle, M. Nicolaus, A new snow thermodynamic scheme for large-scale sea-ice models, *Ann. Glaciol.* 52 (57) (2011) 337–346.
- [17] S.J. Prinsenberg, I.K. Peterson, J.S. Holladay, L. Lalumiere, Snow and ice thickness properties of Lake Melville, a Canadian fjord located along the labrador coast, in: Proceedings of the 21st International Offshore and Polar Engineering Conference (ISOPE), Maui, Hawaii, USA, June 19–24, 2011, pp. 935–941.
- [18] R.T. Tonboe, G. Dybkjaer, J.L. Hoyer, Simulations of the snow covered sea ice surface temperature and microwave effective temperature, *Tellus* 63A (2011) 1,028–1,037.
- [19] J. Haapala, M. Lensu, M. Dumont, A.H.H. Renner, M.A. Granskog, S. Gerland, Small-scale horizontal variability of snow, sea-ice thickness and freeboard in the first-year ice region north of Svalbard, *Ann. Glaciol.* 54 (62) (2013) 261–266.
- [20] M.S. Raleigh, C.C. Landry, M. Hayashi, W.L. Quinton, J.D. Lundquist, Approximating snow surface temperature from standard temperature and humidity data: new possibilities for snow model and remote sensing evaluation, *Water Resour. Res.* 49 (2013), 8,053–058,069.
- [21] K. Castro-Morales, R. Ricker, R. Gerdes, Regional distribution and variability of model-simulated Arctic snow on sea ice, *Polar Science* 13 (2017) 33–49.
- [22] R. Kwok, N.T. Kurtz, L. Brucker, A. Ivanoff, T. Newman, S.L. Farrell, J. King, S. Howell, M.A. Webster, J. Paden, C. Leuschen, J.A. MacGregor, J. Richter-Menge, J. Harbeck, M. Tschudi, Intercomparison of snow depth retrievals over Arctic sea ice from radar data acquired by Operation IceBridge, *Cryosphere* 11 (2017), 2,571–572,593.
- [23] X. Lu, Y. Hu, Z. Liu, S. Rodier, M. Vaughan, P. Lucke, C. Treppte, J. Pelon, Observations of Arctic snow and sea ice cover from CALIOP lidar measurements, *Remote Sens. Environ.* 194 (2017) 248–263.
- [24] I. Merkouriadi, B. Cheng, R.M. Graham, A. Rösel, M.A. Granskog, Critical role of snow on sea ice growth in the atlantic sector of the arctic ocean, *Geophys. Res. Lett.* 44 (2017) 10,479–10,485.
- [25] A.R. Mitchell, D.F. Griffiths, *The Finite Difference Method in Partial Differential Equations*, John Wiley, New York, USA, 1980.
- [26] A. MacKinnon, “The Dufort-Frankel Method,” Accessed on the World Wide Web, 2015. <http://www.cmath.ph.ic.ac.uk/people/a.mackinnon/Lectures/compphys/no3e35.html>. (Accessed 5 June 2018).
- [27] I.D. Turnbull, R.S. Taylor, Coastal labrador land-fast ice; relative influences of the thermodynamic forcings on the break-up and effects of clouds, humidity, and wind, *J. Ocean Technol.* 13 (1) (2018) 76–105.